Commun Nonlinear Sci Numer Simulat 138 (2024) 108231

Contents lists available at ScienceDirect

Communications in Nonlinear Science and Numerical Simulation

journal homepage: www.elsevier.com/locate/cnsns

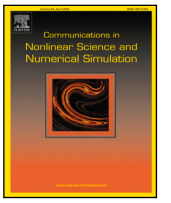

Research paper

An adaptive non-uniform L2 discretization for the one-dimensional space-fractional Gray–Scott system

P. Yuan *, P.A. Zegeling

Utrecht University, Budapestlaan 6, 3584 CD Utrecht, The Netherlands

ARTICLE INFO

Keywords:
Fractional Laplacian
L2 method
Moving mesh method
Gray–Scott model

ABSTRACT

This paper introduces a new numerical method for solving space-fractional partial differential equations (PDEs) on non-uniform adaptive finite difference meshes, considering a fractional order $\alpha \in (1,2)$ in one dimension. The fractional Laplacian in PDE is computed by using Riemann–Liouville (R–L) derivatives, incorporating a boundary condition of the form $u = 0$ in $\mathbb{R}\backslash\Omega$. The proposed approach extends the L2 method to non-uniform meshes for calculating the R–L derivatives. The spatial mesh generation employs adaptive moving finite differences, offering adaptability at each time step through grid reallocation based on previously calculated solutions. The chosen mesh movement technique, moving mesh PDE-5 (MMPDE-5), demonstrates rapid and efficient mesh movement. The numerical solutions are obtained by applying the non-uniform L2 numerical scheme and the MMPDE-5 method for moving meshes automatically. Two numerical experiments focused on the space-fractional heat equation validate the convergence of the proposed scheme. The study concludes by exploring patterns in equations involving the fractional Laplacian term within the Gray–Scott system. It reveals self-replication, travelling wave, and chaotic patterns, along with two distinct evolution processes depending on the order α: from self-replication to standing waves and from travelling waves to self-replication.

1. Introduction

Fractional differential equations garner significant interest in both numerical and theoretical studies due to the enhanced accuracy of fractional derivatives in describing memory and hereditary properties across various materials [1] and processes [2,3]. One development in this field is the extension of the Laplacian operator to fractional orders, a concept named after Marcel Riesz, distinguished for substantial contributions to functional analysis and potential theory [4]. The Riesz fractional Laplacian is commonly denoted by $-(-\Delta)^{\frac{\alpha}{2}}$, where α is the fractional order [5]. In the context of partial differential equations, the Riesz fractional Laplacian arises in problems involving non-local effects and has applications in areas such as physics, finance, and image processing.

The Riesz fractional Laplacian operator can be viewed as a nonlocal generalization of the integer-order Laplacian. One of the differences between the Riesz fractional Laplacian and the ordinary Laplacian is their behaviour in boundary value problems. For a function u defined on $\mathbb{R}$, the Riesz fractional Laplacian (also referred to the integral fractional Laplacian [6]) in can be defined via a singular integral

$$(-\Delta)^{\frac{\alpha}{2}} u(x) = C(1,\alpha)\ \text{P.V.} \int_{\mathbb{R}} \frac{u(x)-u(y)}{|x-y|^{1+\alpha}} dy,\ \ \alpha \in (0,2), \tag{1}$$

* Corresponding author.
E-mail addresses: p.yuan@uu.nl (P. Yuan), P.A.Zegeling@uu.nl (P.A. Zegeling).

https://doi.org/10.1016/j.cnsns.2024.108231
Received 13 March 2024; Received in revised form 15 July 2024; Accepted 16 July 2024
Available online 20 July 2024

where $C(1,\alpha) = \frac{2^\alpha \Gamma(\frac{1+\alpha}{2})}{\sqrt{\pi}|\Gamma(-\frac{\alpha}{2})|}$ and P.V. denotes the principal value of the integral. Different from solving a usual diffusion equation problem, we should note that the domain of $(-\Delta)^{\frac{\alpha}{2}}$ consists of functions defined on $\mathbb{R}$, rather than a finite domain Ω, *i.e.* PDEs with the boundary type $u|_{\partial\Omega} = 0$ are ill-posed. This issue is addressed by employing the regional Laplacian, which differs from the Riesz definition, even if $u(x) \equiv 0$ for $x \in \mathbb{R}\backslash\Omega$, see [5,7,8]. Therefore, a well-posed problem defined on $\mathbb{R}$ is given by

$$\begin{cases} \dfrac{\partial u}{\partial t} = -(-\Delta)^{\frac{\alpha}{2}} u + f(u,x,t), \ \ x \in \Omega, \\ u = 0 \ \ \text{in } \mathbb{R}\backslash\Omega. \end{cases} \tag{2}$$

For simplicity, we use the fractional Laplacian instead of the Riesz fractional Laplacian in subsequent discussions. Normally, giving a discretized form of the fractional Laplacian operator is difficult since it is complicated to calculate the integral in (2) directly. Instead, we use the property that the fractional Laplacian is equivalent to the Riesz potential for smooth functions, and Riesz could be represented as the combination of the left and right side Riemann–Liouville fractional derivatives. Thus, solving the fractional Laplacian is transformed into making use of the Riemann–Liouville fractional derivative. If we further constrain the smoothness of the integrated function u within a open bounded domain Ω, it will lead the Riesz–Liouville derivative to degenerate into a fractional derivative neglecting boundary effects, *i.e.*, the Caputo derivative [5,9]. These will be discussed in Section 2 detailed.

It is known that, for $u \in C^m(\bar{\Omega})$ with order $m-1 < \alpha < m$, the Riemann–Liouville derivative exists and coincides with the Grünwald–Letnikov derivative. This relationship between the Riemann–Liouville and Grünwald–Letnikov definitions allows the use of the Riemann–Liouville definition during the problem formulation, and then the Grünwald–Letnikov definition for obtaining the numerical solution [3,10], *i.e.*, using a numerical algorithm for the integral part of the Riemann–Liouville derivatives leads to the Grünwald–Letnikov derivatives. For $1 < \alpha < 2$, we call this L2 method, which is introduced in Section 3. The L2 method, recognized for its efficacy in discretizing Riemann–Liouville derivatives, has been extensively investigated on the uniform meshes by scholars such as [3,9,11]. While there has been considerable research on the L2 method applied to non-uniform meshes, the focus has predominantly centred on the fractional time derivative to overcome the numerical oscillations possibly occur near the initial time [12,13]. Similar to spatial cases, for steep and moving solutions of PDEs, uniform L2 method requires a significantly high number of mesh points around the abrupt changes of solutions to accurately represent the changes in the solution. To improve the computational efficiency and accuracy, in this paper, we generalize the L2 method to non-uniform meshes for spatial Riemann–Liouville derivatives of order $1 < \alpha < 2$ by using a central difference approximation. This approach offers flexibility in mesh construction and different updating techniques for enhanced numerical performance.

After we have constructed the generalized L2 algorithm, in Section 4, we present a mesh generating technique called Moving Mesh PDE (MMPDE). This technique is a widely recognized mesh generation approach extensively explored by researchers like Huang and Russell, among others [14–16]. MMPDE operates on the fundamental principle of equidistribution, enabling the automatic allocation of meshes at each time step. This characteristic distinguishes it from uniform mesh approaches, as it permits a more precise numerical solution with reduced mesh points across various scenarios, particularly in cases involving solutions of partial differential equations with abrupt discontinuities or steep fronts. In this article, we use MMPDE-5 for mesh adaptation due to its notable ease of discretization and also adaptability in high-dimensional contexts [17,18]. MMPDE-5 can be regarded as an extended version of the equidistribution principle, contributing to its practicality in a variety of computational settings.

Within this study, our aim is to solve space-fractional PDE problems and apply the numerical method to a specific nonlinear fractional PDE model: the space-fractional Gray–Scott system. The ordinary (integer-order) Gray–Scott model, a representative of classical reaction–diffusion models, can create a variety of patterns found in nature, such as spots, spot replication, stripes, and travelling waves [19,20]. Its pattern formation has been extensively studied by many researchers [21,22]. In the section on numerical experiments, we first apply the adaptive L2 (L2-MMPDE-5) algorithm to (2) in two specific models: a fractional heat equation and a fractional heat equation with a source, and the results show the numerical convergence of the method. Then we proceed to numerically solve the equations represented by the Gray–Scott system involving the fractional Laplacian term. In these experiments, five patterns of the fractional Gray–Scott system are presented: self-replication, travelling waves, periodic solutions, chaotic behaviour, and bifurcations between stable and self-replicating patterns.

2. Preliminaries

In this paper we consider the fractional Laplacian as defined via Riemann–Liouville fractional derivatives of order $\alpha \in (1,2)$. Here, we introduce some main definitions of fractional derivatives that we will use. For a open bounded set $\Omega = (a,b)$ or $\Omega = \mathbb{R}$, the Riemann–Liouville fractional derivatives and the Caputo fractional derivatives are defined as follows [23]:

Riemann–Liouville fractional derivatives. The left and right Riemann–Liouville derivatives of order $\alpha > 0$ for a function $u(x), x \in \Omega$ are given by

$${}_{RL}D^{\alpha}_{a,x}u(x) = \frac{1}{\Gamma(m-\alpha)}\frac{d^m}{dx^m}\int_a^x (x-s)^{m-\alpha-1}u(s)ds, \tag{3}$$

$${}_{RL}D^{\alpha}_{x,b}u(x) = \frac{(-1)^m}{\Gamma(m-\alpha)}\frac{d^m}{dx^m}\int_x^b (s-x)^{m-\alpha-1}u(s)ds, \tag{4}$$

respectively, where $m-1 \le \alpha < m$ with $m > 0$ being an integer.

Caputo fractional derivatives. The left and right Caputo derivatives of order $\alpha > 0$ for a function $u(x), x \in \Omega$ are given by

$$ {}_C D^{\alpha}_{a,x} u(x) = \frac{1}{\Gamma(m-\alpha)} \int_a^x (x-s)^{m-\alpha-1} u^{(m)}(s) ds, \tag{5} $$

$$ {}_C D^{\alpha}_{x,b} u(x) = \frac{(-1)^m}{\Gamma(m-\alpha)} \int_x^b (s-x)^{m-\alpha-1} u^{(m)}(s) ds, \tag{6} $$

respectively, where $m-1 \le \alpha < m$ with $m > 0$ being an integer.

Lemma 2.1. *Let $x \in \bar{\Omega}, \alpha \in \mathbb{R}$. Then the Riemann–Liouville and Caputo fractional derivatives are related as follows:*

$$ {}_{RL} D^{\alpha}_{a,x} u(x) = \sum_{k=0}^{m-1} \frac{u^{(k)}(a)(x-a)^{k-\alpha}}{\Gamma(k+1-\alpha)} + {}_C D^{\alpha}_{a,x} u(x), \tag{7} $$

$$ {}_{RL} D^{\alpha}_{x,b} u(x) = \sum_{k=0}^{m-1} \frac{u^{(k)}(b)(b-x)^{k-\alpha}}{\Gamma(k+1-\alpha)} + {}_C D^{\alpha}_{x,b} u(x). \tag{8} $$

Proof. See [23]. □

Lemma 2.1 shows that for $\alpha \in \mathbb{R}$, if $u(x) \in \{u \in \mathbf{C}^{[\alpha]} : u^{(k)}(x)|_{\partial\Omega} = 0, k \le [\alpha]\}$, then the left (right) Riemann–Liouville derivative is equivalent to the left (right) Caputo derivative.

The Riesz derivative. Suppose $u \in \mathbf{C}^{[\alpha]}_b(\mathbb{R}) := \{u \in \mathbf{C}^k(\mathbb{R}) : \frac{d^k u}{dx^k}$ is continuous and bounded, $k \le [\alpha]\}$ with $\alpha \in (0,1) \cup (1,2)$. Then, we have the following relation between the Riesz derivative and the Riemann–Liouville derivatives [4]

$$ \frac{\partial^{\alpha}}{\partial |x|^{\alpha}} u(x) = -\frac{1}{2\cos(\alpha\pi/2)} ({}_{RL} D^{\alpha}_{a,x} + {}_{RL} D^{\alpha}_{x,b}) u(x). \tag{9} $$

Furthermore, if $u \in S(\mathbb{R}) := \left\{ u \in C^{\infty}(\mathbb{R}) \mid \forall i, j \in \mathbb{N}, \ \sup_{x \in \mathbb{R}} \left| x^i (f^{(j)}(x) \right| < \infty \right\})$ with $\alpha \in (0,1) \cup (1,2)$, the fractional Laplacian $-(-\Delta)^{\frac{\alpha}{2}}$ defined in (1) is equivalent to the Riesz derivative: [5,9,23]

$$ -(-\Delta)^{\frac{\alpha}{2}} u(x) = \frac{\partial^{\alpha}}{\partial |x|^{\alpha}} u(x), \ x \in \mathbb{R}. \tag{10} $$

Theorem 2.2. *For a finite domain $\Omega = (a,b)$ and a function $u \in C^{[\alpha]}_0(\Omega) := \{u \in C^{[\alpha]}(\Omega) : u|_{\mathbb{R}\setminus\Omega} = 0\}$ with $\alpha \in (0,1) \cup (1,2)$, the following equality holds:*

$$ -(-\Delta)^{\frac{\alpha}{2}} u(x) = -\frac{1}{2\cos(\alpha\pi/2)} ({}_{RL} D^{\alpha}_{a,x} + {}_{RL} D^{\alpha}_{x,b}) u(x). \tag{11} $$

If, furthermore, $\frac{du}{dx}$ vanishes in $\mathbb{R}\setminus\Omega$, then:

$$ -(-\Delta)^{\frac{\alpha}{2}} u(x) = -\frac{1}{2\cos(\alpha\pi/2)} ({}_C D^{\alpha}_{a,x} + {}_C D^{\alpha}_{x,b}) u(x). \tag{12} $$

Proof. Applying Lemma 2.1 and (9) directly. □

Remark 2.1. Note that if $u \in S(\mathbb{R})$ for $\alpha \uparrow 2$ and $\alpha \downarrow 0$, the fractional Laplacian equals the Riesz derivative and becomes the ordinary Laplacian operator Δ and $u(x)$ itself respectively [24,25]:

$$ \lim_{\alpha \uparrow 2} \left[-(-\Delta)^{\frac{\alpha}{2}} u(x) \right] = \Delta u(x) \text{ and } \lim_{\alpha \downarrow 0} [-(-\Delta)^{\frac{\alpha}{2}} u(x)] = -u(x). $$

And for $\alpha = 1$, the fractional Laplacian becomes the Hilbert transform $\mathcal{H}$ of the first derivative [26,27]:

$$ -(-\Delta)^{\frac{1}{2}} u(x) = -\mathcal{H}(\frac{d}{dx} u(x)). $$

Based on Theorem 2.2, we construct a numerical scheme: the non-uniform L2 method to discretize the fractional operator $(-\Delta^{\frac{\alpha}{2}})$ by approximating the Riesz $\frac{\partial^{\alpha}}{\partial |x|^{\alpha}}$, making use of approximations for the left (3) and right Riemann–Liouville derivatives (4).

3. The L2 method for discretizing the Riesz derivative on non-uniform spatial meshes

In this section, algorithms for implementing integro-differentiation to fractional order $1 < \alpha < 2$ are discussed and evaluated. The L2 method, recognized for its efficacy in discretizing Riemann–Liouville derivatives, has been extensively investigated on uniform meshes by scholars such as [3,9–11]. While there has been considerable research on the L2 method applied to non-uniform meshes, the focus has predominantly centred on the fractional time derivative, as exemplified by studies by [12,13]. Inspired by these three works, we generalize the L2 method to non-uniform meshes for spatial Riemann–Liouville derivatives and derive its consistence error.

Based on Lemma 2.1, it is evident that the accuracy of the approximations for Riemann–Liouville derivatives fundamentally depends on the approximations of the Caputo derivatives. As a consequence, we present the L2 non-uniform scheme specifically tailored for the Caputo derivatives. For a finite domain $\Omega = (a, b)$ and $u \in \mathbf{C}_0^{[\alpha]}(\Omega)$, we consider a set of $N+1$ mesh points, denoted by $\{x_n\}_{n=0}^N$, forming the $\overline{\Omega}$, where x_0 and x_N are the boundary points of Ω: $x_0 = a, x_N = b$.

$$
\begin{aligned}
{}_C D^{\alpha}_{a,x} u(x_n) &= \frac{1}{\Gamma(2-\alpha)} \int_a^{x_n} (x_n - s)^{1-\alpha} u''(s) ds \qquad n = 1, \dots, N-1 \\
&= \frac{1}{\Gamma(2-\alpha)} \sum_{k=1}^{n} \int_{x_{k-1}}^{x_k} (x_n - s)^{1-\alpha} u''(s) ds.
\end{aligned}
$$

Within each subinterval $[x_{k-1}, x_k]$, we employ quadratic interpolation, denote as $\Pi_{2,k} u(x)$, with the points $(x_{k-1}, u(x_{k-1}))$, $(x_k, u(x_k))$, and $(x_{k+1}, u(x_{k+1}))$ to approximate $u(x)$. Taking second derivatives to $\Pi_{2,k} u(x)$ gives a central difference approximation to $u''(x_k)$. Consequently, the approximation of the left Caputo derivative in Ω is determined by,

$$
\begin{aligned}
{}_C D^{\alpha}_{a,x} u(x_n) &\approx \frac{2}{\Gamma(2-\alpha)} \sum_{k=1}^{n} \left(\frac{u(x_{k-1})}{h_{k-1}(h_{k-1}+h_k)} - \frac{u(x_k)}{h_k h_{k-1}} + \frac{u(x_{k+1})}{h_k(h_k + h_{k-1})} \right) \int_{x_{k-1}}^{x_k} (x_n - s)^{1-\alpha} ds \\
&= \frac{2}{\Gamma(3-\alpha)} \sum_{k=1}^{n} \left(\frac{u(x_{k-1})}{h_{k-1}(h_{k-1}+h_k)} - \frac{u(x_k)}{h_k h_{k-1}} + \frac{u(x_{k+1})}{h_k(h_k + h_{k-1})} \right) \left((x_n - x_{k-1})^{2-\alpha} - (x_n - x_k)^{2-\alpha} \right),
\end{aligned} \tag{13}
$$

where the mesh spacings $h_k = x_{k+1} - x_k,\ k = 0, \dots, n-1$.

Similar for the right Caputo derivative, on each subinterval $[x_k, x_{k+1}]$ we have

$$
\begin{aligned}
{}_C D^{\alpha}_{x,b} u(x_n) &= \frac{1}{\Gamma(2-\alpha)} \sum_{k=n}^{N-1} \int_{x_k}^{x_{k+1}} (s - x_n)^{1-\alpha} u''(s) ds, \qquad n = 1, \dots, N-1 \\
&\approx \frac{2}{\Gamma(3-\alpha)} \sum_{k=n}^{N-1} \left(\frac{u(x_{k-1})}{h_{k-1}(h_{k-1}+h_k)} - \frac{u(x_k)}{h_k h_{k-1}} + \frac{u(x_{k+1})}{h_k(h_k + h_{k-1})} \right) \left((x_{k+1} - x_n)^{2-\alpha} - (x_k - x_n)^{2-\alpha} \right),
\end{aligned} \tag{14}
$$

Remark 3.1. Note that as $\alpha \uparrow 2$ the generalized L2 method will reduce to the central 3-point approximation for $u''(x)$ since only $(x_n - x_{n-1})^{2-\alpha}$ will exist and approach to 1, same for the right-side Caputo derivative.

Based on the definition for the Riesz derivative representation of the fractional Laplacian in Eqs. (9), we combine the left (13) and right (14) derivatives. It gives the non-uniform L2 approximation to the fractional Laplacian in one dimension.

We will apply this scheme with the adaptive moving mesh method described in the next section to obtain a full numerical scheme for solving space fractional PDEs on adaptive finite difference meshes. To show the method is consistent consider the following Lemma.

Lemma 3.1. *For $1 < \alpha < 2$, and $u \in C^3[a, b]$, it holds that*

$$
\begin{aligned}
\int_a^{x_n} (x_n - s)^{1-\alpha} u''(s) ds &= 2 \sum_{k=1}^{n} \left(\frac{u(x_{k-1})}{h_{k-1}(h_{k-1}+h_k)} - \frac{u(x_k)}{h_k h_{k-1}} + \frac{u(x_{k+1})}{h_k(h_k + h_{k-1})} \right) \\
&\quad \times \int_{x_{k-1}}^{x_k} (x_n - s)^{1-\alpha} ds + R_n,\ 1 \le n \le N-1
\end{aligned} \tag{15}
$$

with

$$
|R_{L,n}| \le \frac{u''_M}{3(2-\alpha)} \left(\frac{h_M^2}{h_m} \left((x_n - a)^{2-\alpha} - h_{n-1}^{2-\alpha} \right) + \frac{h_{n-1}^2 + h_n^2}{h_{n-1} + h_n} h_{n-1}^{2-\alpha} \right)
$$

where $u''_M = \max_{a \le x \le x_n} |u'''(x)|$ and $h_M = \max_{0 \le k \le n-1} h_{k-1}, h_m = \min_{0 \le k \le n-1} h_{k-1}$.

Proof. We first use $\Pi_{2,k} u$ to approximate u on each interval $[x_k, x_{k+1}]$, where

$$
\Pi_{2,k} u(x) = u(x_{k-1}) \frac{(x - x_k)(x - x_{k+1})}{h_{k-1}(h_{k-1}+h_k)} + u(x_k) \frac{(x - x_{k-1})(x - x_{k+1})}{-h_{k-1} h_k} + u(x_{k+1}) \frac{(x - x_{k-1})(x - x_k)}{h_k(h_{k-1}+h_k)}
$$

is the quadratic interpolation of $u(x)$ using three points $(x_{k-1}, u(x_{k-1})), (x_k, u(x_k))$ and $(x_{k+1}, u(x_{k+1}))$. And the second derivative of $\Pi_{2,k} u(s)$ is given by

$$
(\Pi_{2,k} u(s))'' = 2 \left(\frac{u(x_{k-1})}{h_{k-1}(h_{k-1}+h_k)} - \frac{u(x_k)}{h_k h_{k-1}} + \frac{u(x_{k+1})}{h_k(h_k + h_{k-1})} \right),
$$

which actually is the central finite difference of the $u''(x_k)$ on (x_{k-1}, x_{k+1}). Therefore, the truncation error $R_L(k)$ can be estimated by

$$\begin{aligned}|R_L(k)| &= \left|u''(x_k) - 2\left(\frac{u(x_{k-1})}{h_{k-1}(h_{k-1}+h_k)} - \frac{u(x_k)}{h_k h_{k-1}} + \frac{u(x_{k+1})}{h_k(h_k+h_{k-1})}\right)\right| \\ &= \frac{1}{3}\left|\frac{h_{k-1}^2}{h_{k-1}+h_k}u'''(\xi_1) - \frac{h_k^2}{h_{k-1}+h_k}u'''(\xi_2)\right|,\ \xi_1 \in (x_{k-1}, x_k),\ \xi_2 \in (x_k, x_{k+1}).\end{aligned} \tag{16}$$

Now we analyse the error bounds on the interval $[a, x_n]$. Write the integral as

$$\int_a^{x_n}(x_n-s)^{1-\alpha}u''(s)ds = \int_a^{x_{n-1}}(x_n-s)^{1-\alpha}u''(s)ds + \int_{x_{n-1}}^{x_n}(x_n-s)^{1-\alpha}u''(s)ds$$

For the first integral on the right side we have

$$\begin{aligned}\int_a^{x_{n-1}}(x_n-s)^{1-\alpha}u''(s)ds &= \sum_{k=1}^{n-1}\int_{x_{k-1}}^{x_k}(x_n-s)^{1-\alpha}u''(s)ds \\ &= \sum_{k=1}^{n-1}(\Pi_{2,k}u(s))''\int_{x_{k-1}}^{x_k}(x_n-s)^{1-\alpha}ds + R_{L,n-1},\end{aligned}$$

then it gives

$$\begin{aligned}|R_{L,n-1}| &= \left|\sum_{k=1}^{n-1}R_L(k)\int_{x_{k-1}}^{x_k}(x_n-s)^{1-\alpha}ds\right| \le \sum_{k=1}^{n-1}|R_L(k)|\int_{x_{k-1}}^{x_k}(x_n-s)^{1-\alpha}ds \\ &\le \frac{1}{3}\left(\max_{a\le x\le x_n}|u'''(x)|\frac{\max_{0\le i\le n-1}h_i^2}{\min_{0\le i\le n-1}h_i}\right)\int_a^{x_{n-1}}(x_n-s)^{1-\alpha}ds \\ &= \frac{1}{3(2-\alpha)}\left(\max_{a\le x\le x_n}|u'''(x)|\frac{\max_{0\le i\le n-1}h_i^2}{\min_{0\le i\le n-1}h_i}\right)\left((x_n-a)^{2-\alpha} - h_{n-1}^{2-\alpha}\right)\end{aligned}$$

Similarly, for $R_L(n)$ we have

$$\begin{aligned}|R_L(n)| &\le \max_{x_{n-1}\le x\le x_{n+1}}|u'''(x)|\int_{x_{n-1}}^{x_n}(x_n-s)^{1-\alpha}u''(s)ds \\ &= \frac{1}{3(2-\alpha)}\left(\max_{x_{n-1}\le x\le x_{n+1}}|u'''(x)|\frac{h_{n-1}^2+h_n^2}{h_{n-1}+h_n}\right)h_{n-1}^{2-\alpha}.\end{aligned}$$

As the $|R_{L,n}|$ is bounded by $|R_{L,n-1}| + |R_L(n)|$, this yields the results. □

By using similar analysis for the right-side,

$$\begin{aligned}\int_{x_n}^b(s-x_n)^{1-\alpha}u''(s)ds &= 2\sum_{k=n}^{N-1}\left(\frac{u(x_{k-1})}{h_{k-1}(h_k+h_{k-1})} - \frac{u(x_k)}{h_{k-1}h_k} + \frac{u(x_{k+1})}{h_k(h_k+h_{k-1})}\right) \\ &\quad\times\int_{x_k}^{x_{k+1}}(s-x_n)^{1-\alpha}ds + R_{R,n},\ 1\le n\le N-1\end{aligned} \tag{17}$$

it gives

$$|R_{R,n}| \le \frac{u_M'''}{3(2-\alpha)}\left(\frac{h_M^2}{h_m}\left((b-x_n)^{2-\alpha} - h_n^{2-\alpha}\right) + \frac{h_{n-1}^2+h_n^2}{h_{n-1}+h_n}\right)h_n^{2-\alpha},$$

where $u_M''' = \max_{x_n\le x\le b}|u'''(x)|$ and $h_M = \max_{n+1\le k\le N-1}h_{k-1}, h_m = \min_{n+1\le k\le N-1}h_{k-1}$.

Remark 3.2. If there exists a finite constant h such that $\frac{\max_{0\le k\le N-1}h_{k-1}}{\min_{0\le k\le N-1}h_{k-1}} \le h$, then the sequence of meshes is referred to as quasi-uniform. For $h = 1$, it holds that $h_n = h = \frac{b-a}{N}$ for all $n = 1, \dots, N-1$, then $R_L(k)$ in (16) is bounded by

$$|R_L(k)| \le \frac{h^2}{3}\max_{x_{k-1}\le x\le x_{k+1}}|u''''(x)|,$$

and the left-side error

$$\begin{aligned}|R_{L,n}| &\le |R_{L,n-1}| + |R_L(n)| \\ &\le \frac{h^2}{3}\max_{a\le x\le x_n}|u''''(x)|\int_a^{x_{n-1}}(x_n-s)^{1-\alpha}ds + \frac{h^{3-\alpha}}{3(2-\alpha)}\max_{x_{n-1}\le x\le x_{n+1}}|u'''(x)|\end{aligned} \tag{18}$$

$$\leq \frac{h^2}{3}\max_{a\leq x\leq x_n}|u''''(x)|(a-x_{n-1})h_{n-1}^{1-\alpha}+\frac{h^{3-\alpha}}{3(2-\alpha)}\max_{x_{n-1}}u'''(x) \tag{19}$$

$$\leq \frac{h^{3-\alpha}}{3}\left(\max_{a\leq x\leq x_n}|u''''(x)|(a-x_{n-1})+\frac{\max_{x_{n-1}\leq x\leq x_{n+1}}|u'''(x)|}{2-\alpha}\right).$$

Similar analysis can be done for the right-side errors. Thus we conclude that (15) and (17) reduce to a uniform finite difference method with the truncation order $O(h^{3-\alpha})$ [11].

For simplicity, we write (13) and (14) into the computational format (which has been used in the codes). For a left-side Caputo derivative, we denote

$$A_L(i,j)=(x_i-x_{j-1})^{2-\alpha}-(x_i-x_j)^{2-\alpha},\ 1\leq i\leq j\leq N-1,$$

$$H(i,j)=\begin{cases}\dfrac{1}{h_{i-1}(h_{i-1}+h_i)}, & j=i,\\ -\dfrac{1}{h_ih_{i-1}}, & j=i+1,\ \text{with } 1\leq i\leq N-1,\\ \dfrac{1}{h_i(h_{i-1}+h_i)}, & j=i+2,\end{cases}$$

therefore, (13) can be represented as

$${}_C D^{\alpha}_{a,x}U^{\intercal}=\frac{2}{\Gamma(3-\alpha)}(A_LH\bar{U}^{\intercal}+R_L), \tag{20}$$

where $U=[u_1,\dots,u_{N-1}]$, $\bar{U}=[u_0,U,u_N]$ and $R_L=[R_{L,1},\dots,R_{L,N-1}]$. Similar for the right-side Caputo derivative, denoting that

$$A_R(i,j)=(x_{j+1}-x_i)^{1-\alpha}-(x_j-x_i)^{2-\alpha},\ 1\leq i\leq j\leq N-1,$$

then (14) is represented as

$${}_C D^{\alpha}_{x,b}U^{\intercal}=\frac{2}{\Gamma(3-\alpha)}(A_RH\bar{U}^{\intercal}+R_R), \tag{21}$$

where $R_R=[R_{R,1},\dots,R_{R,N-1}]$. The results of Lemma 3.1 prove the following Theorem which shows the consistency of the generalized L2 method.

Theorem 3.2. *For $1<\alpha<2$, and $u\in C^3[a,b]$, it holds that*

$${}_C D^{\alpha}_{a,x}u(x_n)+{}_C D^{\alpha}_{x,b}u(x_n)=\frac{2}{\Gamma(3-\alpha)}[\left(A_LH+A_RH\right)\bar{U}^{\intercal}]_n+R_n, \tag{22}$$

where $[\cdot]_n$ denotes its $n-$th entry and R is the truncation error with $|R_n|\leq\frac{2}{\Gamma(3-\alpha)}(|R_{L,n}|+|R_{R,n}|)$.

4. The adaptive moving mesh method

Different from constructing the uniform mesh, the non-uniform mesh is designed to adapt as time progresses. In this paper, adaptivity is determined through the concept of *equidistribution*, ensuring that the mesh dynamically moves to achieve equidistribution at each time step. This approach involves solving a mesh movement equation, represented as $x(t)$, derived from the equidistribution principle, commonly referred to as the adaptive moving method. This procedure is designed to allocate the mesh points in such a way that distances between them are smaller in regions where the target function $u(x)$ have a sudden change, and the distances are larger in regions where $u(x)$ changes mildly at each time-step. The *monitor function* $M(x)$ is introduced to quantify the extent of change in $u(x)$.

The equidistribution principle, proposed by De Boor in 1973 [28], suggests selecting mesh points in a way that equalizes some measure of the solution error over each subinterval. In practice, an effective approach involves choosing a function $M(x)$ that connects the mesh and the physical solution $u(x)$ such that

$$\int_x^a M(x)dx=\xi\int_a^b M(x)dx, \tag{23}$$

where the physical domain x is a coordinate transformation of the logical domain ξ, *i.e.*, $x=x(\xi,t):[0,1]\times[0,T]\to[a,b]\times[0,T]$. The differential form of (23) is given by

$$\frac{\partial}{\partial\xi}\left(M\frac{\partial x}{\partial\xi}\right)=0, \tag{24}$$

which is the Euler–Lagrange equation of the functional

$$I[x]=\frac{1}{2}\int_0^1\left(M\frac{\partial x}{\partial\xi}\right)^2d\xi. \tag{25}$$

4.1. The moving mesh PDE approach

A mesh equation involving mesh speed is referred to as a moving mesh PDE (MMPDE). There are numerous ways of formulating MMPDEs [14,29]. Here we use a idea that the fastest descent direction of $I[x]$ of (25) in the function space is the opposite direction of the first order functional derivative $\frac{\delta I}{\delta x}$. Thus, we define the gradient flow equation

$$\frac{\partial x}{\partial t} = -\frac{P}{\tau}\frac{\delta I}{\delta x}, \tag{26}$$

which defines a flow which converges to the equilibrium state as $t \to \infty$, P is a positive function to be chosen such that the MMPDE has some desired properties and τ is a positive constant, see [17].

By substituting (25) and set $P = \frac{1}{M(x)}$ such that the second-order derivatives change evenly over the domain (so that the MMPDE behaves more like a diffusion equation with an almost constant diffusion coefficient), we derived this so-called MMPDE-5 that will be utilized to move the mesh

$$\frac{\partial x}{\partial t} = \frac{1}{\tau}\frac{\partial}{\partial \xi}\left(M\frac{\partial x}{\partial \xi}\right), \tag{27}$$

$$x(0,t) = a,\ \ x(1,t) = b, \tag{28}$$

where τ is a positive parameter for adjusting the response time of mesh movement to changes in monitor function. The smaller of τ chosen, the faster mesh move towards the equidistribution rule. Since $\frac{1}{\tau}\left(Mx_{\xi}\right)_{\xi}$ plays the role of a driving force for mesh movement and provides the mechanism to pull the mesh back towards equidistribution of the monitor function M when it drifts away from equidistribution. If $x = x(\xi, t)$ is an invertible coordinate transformation, and furthermore, the monitor function M and its time derivative M_t are both bounded, then it is proved in [15] that $x(\xi, t)$ stays of the order $O(\tau)$ close to the minimizer of the functional (25)$x^*(\xi, t)$ as $t \to \infty$ in the L^2 sense.

4.2. Monitor functions

The selection of an appropriate monitor function is pivotal to the success of mesh equidistribution in the adaptive numerical solution of differential equations. Typically, the motivation for selecting the monitor function $M(x)$ is the desire to minimize an error in interpolating a function or in solving a differential equation, as extensively discussed in [15]. In this paper, we primarily employ a so-called *optimal monitor function* denoted as M, which is given by,

$$M = \left(1 + \frac{1}{\gamma}\left|\frac{\partial u}{\partial x}\right|^2\right)^{\frac{1}{3}} \text{ and } \gamma = \left[\frac{1}{b-a}\int_a^b \left(\frac{\partial u}{\partial x}\right)^{\frac{2}{3}} dx\right]^3, \tag{29}$$

for u in the Hilbert space $H^2(a, b)$. The choice of γ is following two criteria [15,18,30]; (i) ensure that the monitor function defined in (29) is invariant under a scaling transformation of u; (ii) for a given mesh $\mathcal{J}_h : x_0 = a < x_2 < \cdots < x_N = b$ on $[a, b]$, ensure that $\sum_i (x_{i+1} - x_i)M_i \le 2(b-a)$. More monitor functions and the derivation of corresponding error bounds can be found in [15].

Smoothing of the monitor functions. The smoothing technique is motivated by the robust moving mesh method of Dori and Drury [16] that is used for those not smooth solutions u, which leads the discrete monitor function computed to change abruptly, slowing down the computation unnecessarily. Direct smoothing of the monitor function is commonly based on the use of an elliptic differential operator (especially the Laplace operator) or an approximation to it. For a given $M(x(\xi))$, a monitor function having higher regularity or a smoother monitor function, $\hat{M}$, can be obtained as the solution of the boundary value problem,

$$\begin{cases} (I - \beta^{-2}\frac{d^2}{d\xi^2})\hat{M} = M, \forall \xi \in (0,1), \\ \frac{d\hat{M}}{d\xi}(0) = \frac{d\hat{M}}{d\xi}(1) = 0, \end{cases} \tag{30}$$

where β is positive constant. If we substitute (30) into (24), then it centred discretized form can be verified that it is exactly the one used in [16] by letting $\sigma = \frac{N^2}{\beta^2}$ and choosing the parameter β such that $\sigma = -\hat{\sigma}(1 + \hat{\sigma})$, where $\hat{\sigma}$ is the measure of the grid's rigidity in [16] and also the spacing grid smoothing parameter κ in [31]. The smoothing defined by (30) is global in the sense that a differential equation must be solved for $\hat{M}$. In this paper, we derive a local smoothing schemes for efficiency by using the Taylor expansion to (30),

$$\hat{M} = \left(I - \beta^{-2}\frac{d^2}{d\xi^2}\right)^{-1} M = \left[I + \left(\beta^{-2}\frac{d^2}{d\xi^2}\right) + \left(\beta^{-2}\frac{d^2}{d\xi^2}\right)^2 + \cdots\right] M,$$

for $\beta \gg 1$. Truncating the expansion and approximating $\frac{d^2}{d\xi^2}$ with a central finite difference we obtain

$$\hat{M}_i = \frac{1}{\beta^2\Delta\xi^2}M_{i+1} + \left(1 - \frac{2}{\beta^2\Delta\xi^2}\right)Mi + \frac{1}{\beta^2\Delta\xi^2}M_{i-1},\ \ i = 2, \ldots, N-1. \tag{31}$$

If $\beta^2\Delta\xi^2 = 4$, it is called weighted *averaging* or *filtering*, that is

$$\begin{cases} \hat{M}_1 = \dfrac{M_1 + M_2}{2}, \\ \hat{M}_i = \dfrac{1}{4}M_{i+1} + \dfrac{1}{2}M_i + \dfrac{1}{4}M_{i-1}, \ i = 2, \dots, N-1, \\ \hat{M}_N = \dfrac{M_{N-1} + M_N}{2}. \end{cases} \tag{32}$$

This could give a smoother non-uniform mesh, making the MMPDE easier to integrate numerically, smoothing of the monitor function is a typical procedure in the context of moving mesh technologies [15].

5. The coupled semi-discrete ODE system

Following the moving mesh PDE as the mesh updating approach, the target equation is transformed from the physical domain to the computational domain using the coordinate transformation (27)–(28) and the chain rule, as follows:

$$\frac{\partial \tilde{u}}{\partial \xi} = \frac{\partial u}{\partial x}\frac{\partial x}{\partial \xi}, \quad \frac{\partial \tilde{u}}{\partial t} = \frac{\partial u}{\partial t} + \frac{\partial u}{\partial x}\frac{\partial x}{\partial t}.$$

Hence, in the new coordinates (ξ, t) Eq. (2) becomes

$$\frac{\partial \tilde{u}}{\partial t} = -\epsilon(-\Delta)^{\frac{\alpha}{2}}\tilde{u} + f(\tilde{u}, x, t) + \frac{\frac{\partial \tilde{u}}{\partial \xi}}{\frac{\partial x}{\partial \xi}}\frac{\partial x}{\partial t}, \tag{33}$$

where $\frac{\partial x}{\partial t}$ is derived from (27)–(28) that determines the mesh speed. Now we combine this mesh generation with the non-uniform L2 scheme (22), giving the numerical scheme for (33). Applying the Method of Lines with central discretization in space to the MMPDE-5 (27)–(28) yields:

$$\begin{cases} \dfrac{dU_n}{dt} = -\dfrac{1}{\Gamma(3-\alpha)\cos(\pi\alpha/2)}[\left(A_L H + A_R H\right)\bar{U}^{\intercal}]_n + \dfrac{U_{n+1} - U_n}{X_{n+1} - X_n}\dfrac{dX_n}{dt} \\ \qquad + (2-\alpha)\left(\dfrac{U_1 - U_0}{X_1 - X_0}(x-a)^{1-\alpha} + \dfrac{U_N - U_{N-1}}{X_N - X_{N-1}}(b-x)^{1-\alpha}\right) + f(U_n, X_n, t), \\ \dfrac{dX_n}{dt} = \dfrac{1}{\tau}\left(\dfrac{X_{n+1} - X_n}{(\Delta\xi)^2}\dfrac{\hat{M}_{n+1} + \hat{M}_n}{2} - \dfrac{X_n - X_{n-1}}{(\Delta\xi)^2}\dfrac{\hat{M}_n + \hat{M}_{n-1}}{2}\right), \\ \hat{M}_n = \dfrac{1}{4}M_{n+1} + \dfrac{1}{2}M_n + \dfrac{1}{4}M_{n-1}, \ n = 2, \dots, N-1, \end{cases} \tag{34}$$

with boundary conditions

$$\begin{cases} U_0 = u(a), \ U_N = u(b), \\ X_0 = a, \ X_N = b, \\ \hat{M}_1 = \dfrac{M_1 + M_2}{2}, \ \hat{M}_N = \dfrac{M_{N-1} + M_N}{2}. \end{cases} \tag{35}$$

If we compute $\hat{M}$ in (34) individually and let $\mathbf{z} = [U_1, \dots, U_{N-1}, X_1, \dots, X_{N-1}]$, then the other two equations in (34) can be expressed in an fully implicit form

$$\Phi(\frac{d\mathbf{z}}{dt}, \mathbf{z}, t) = 0. \tag{36}$$

6. Numerical experiments

Default settings and values of parameters. The above fully implicit ODE system (36) with conditions (35) is solved using the implicit ODE solver `ode15i` (see [32]), where $\hat{M}$ is not involved and calculated at each time step individually. The method of time integration is chosen as the backward differentiation formulas (BDF) with chord iteration (mr25), for which an approximate Jacobian is computed by `ode15i`internally using finite differences. The default values of the parameters for time integration in `ode15i` are used, except for the local time-stepping error tolerances `reltol` and `abstol`. Throughout, we use

$$\texttt{reltol} = 1e-4, \ \texttt{abstol} = 1e-6,$$

unless otherwise stated.

When $x_i(t) - x_{k-1}(t) \approx x_i(t) - x_k(t)$, the evaluation of, $(x_i(t) - x_{k-1}(t))^{2-\alpha} - (x_i(t) - x_k(t))^{2-\alpha}$, is the difference of two nearly equal vectors which leads to noticeable round-off errors. The following simple reformulation using $\mathrm{expm1}(x) = \exp(x) - 1$ and $\mathrm{log1p}(x) = \log(1+x)$ immediately rectifies this instability [33]. For $x_i \le x_k$, we have

$$(x_i(t) - x_{k-1}(t))^{2-\alpha} - (x_i(t) - x_k(t))^{2-\alpha},$$

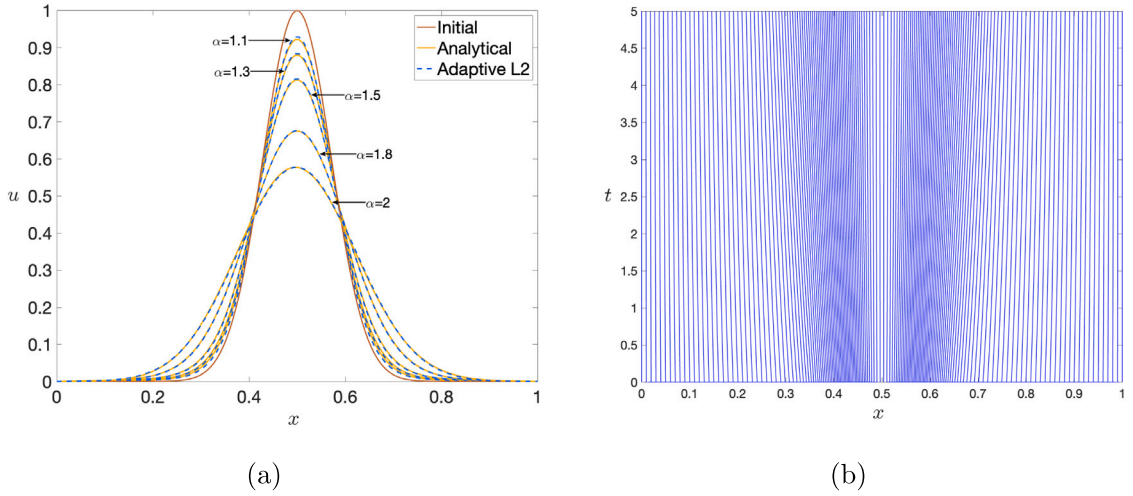

Fig. 1. (a) The numerical solutions of the fractional heat Eq. (38) over 160-moving mesh with $\alpha = 1.1, 1.3, 1.5, 1.8, 2$ at $T = 5$. (b) The mesh movement over a 160-moving mesh for $\alpha = 1.8$ at $T = 5$.

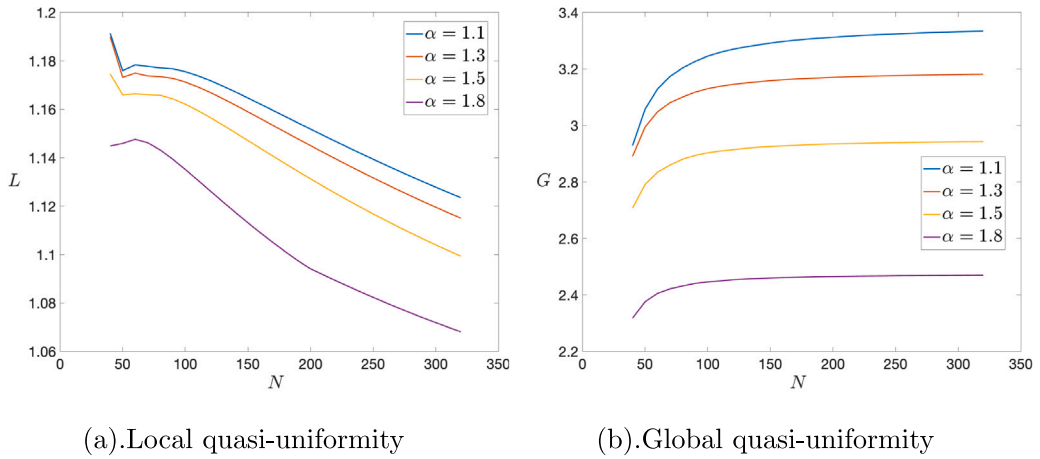

Fig. 2. The local (left) and global (right) quasi-uniformity of the meshes using the adaptive L2 method for (38) are estimated with different values of $\alpha = 1.1, 1.3, 1.5, 1.8$ at $T = 5$.

$$=(x_i(t)-x_{k-1}(t))^{2-\alpha}\left(1-\exp\left(\log\left(\left(\frac{x_i(t)-x_k(t)}{x_i(t)-x_{k-1}(t)}\right)^{2-\alpha}\right)\right)\right),$$
$$=-(x_i(t)-x_{k-1}(t))^{2-\alpha}\text{expm1}\left[(2-\alpha)\text{log1p}\left(\frac{x_{k-1}(t)-x_k(t)}{x_i(t)-x_{k-1}(t)}\right)\right].$$

In order to produce consistent and reasonable meshes, it is natural that we examine the quality of the smoothed equidistribution mesh at a given time, t, we use the local quasi uniformity, which are evaluated by the following expressions

$$L(t)=\max\left\{\frac{h_i(t)}{h_{i-1}(t)},\frac{h_{i-1}(t)}{h_i(t)}\right\},\ G(t)=\frac{\max h_i(t)}{\min h_i(t)},\quad i=1,\ldots,N. \tag{37}$$

We expect that $G(t)$ is bounded, *i.e.* the meshes used in simulations are quasi-uniform. For a mesh satisfying $L(t) \to 1$, which is considered locally quasi-uniform, such meshes typically result in an approximation error of the same asymptotic order as a uniform mesh, see [15,34,35].

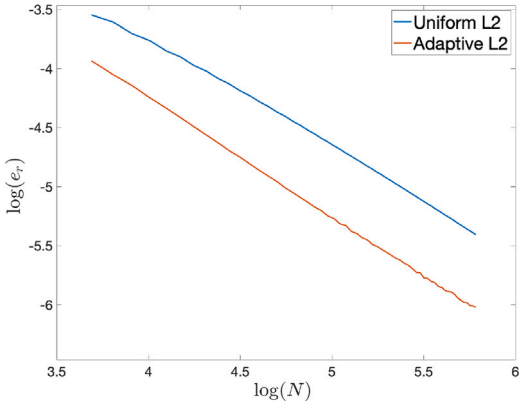

Fig. 3. The relative error e_r of (38) using the L2 method estimated on uniform (blue) and adaptive (red) meshes in the l^∞-norm for $\alpha = 1.5$ at $T = 5$.

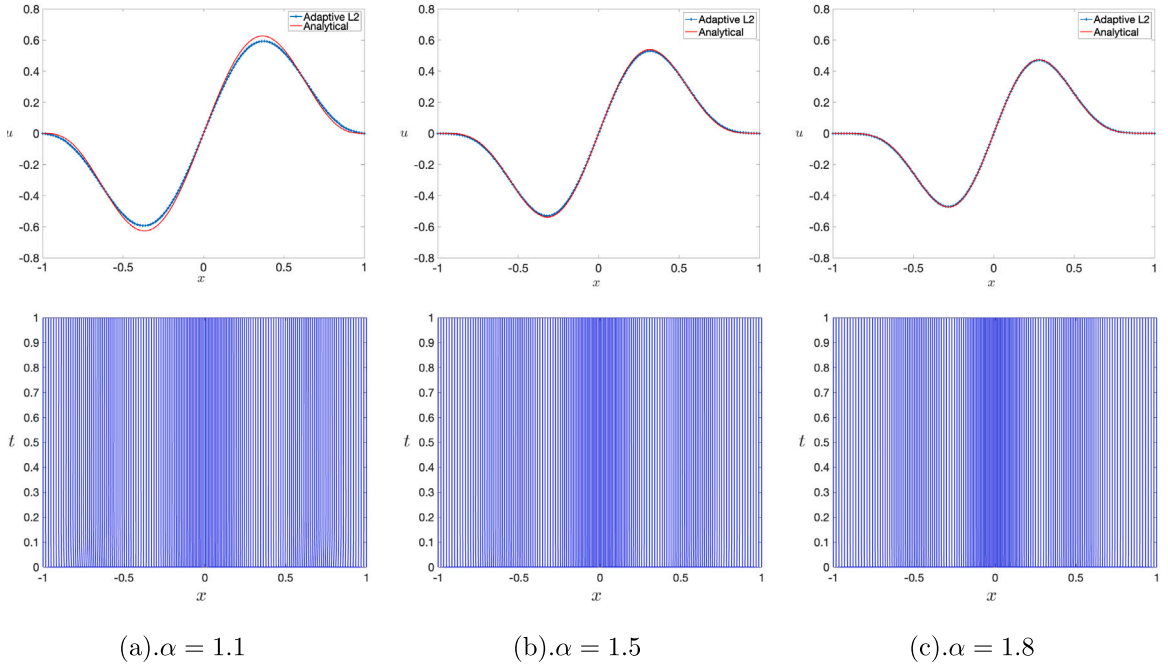

Fig. 4. The numerical solutions and the corresponding mesh movement of (41)–(44) and on a 160-moving mesh for $\alpha = 1.1,\ 1.5,\ 1.8$ at $T = 1$.

6.1. The space-fractional heat equation

Firstly, we consider the space-fractional heat equation

$$\begin{cases} \dfrac{\partial u}{\partial t} = -\epsilon(-\Delta)^{\frac{\alpha}{2}} u & (x,t) \in (0,1)\times[0,T], \\ u = 0 & \text{on } \mathbb{R}\backslash(0,1), \end{cases} \tag{38}$$

where ϵ is the diffusion coefficient. The initial condition is given by

$$u(x,0) = g(x). \tag{39}$$

In this case, we take $\epsilon = 10^{-3}$ and $g(x) = e^{-100(x-\frac{1}{2})^2}$ on $\mathbb{R}$. From [9], we have the analytical solution of (38):

$$u(x,t) = \sum_{n=1}^{\infty} c_n \sin(n\pi x)\, e^{-\epsilon n^\alpha \pi^\alpha t}, \tag{40}$$

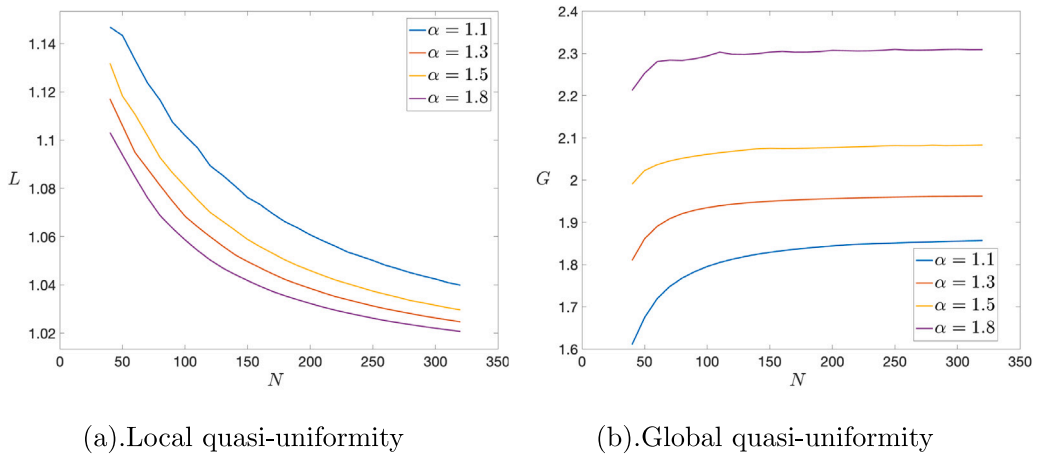

Fig. 5. The local (left) and global (right) quasi-uniformity of the meshes using the adaptive L2 method for (41) are estimated with different values of $\alpha = 1.1, 1.3, 1.5, 1.8$ at $T = 1$.

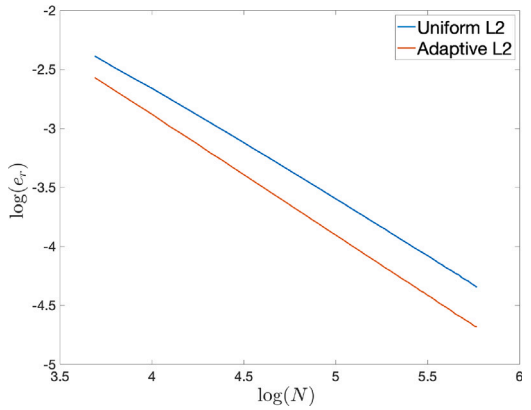

Fig. 6. The relative error e_r of (41) using the L2 method estimated on uniform (blue) and adaptive (red) meshes in the l^∞-norm for $\alpha = 1.5$ at $T = 1$.

with

$$c_n = 2\int_0^1 g(s)\sin(n\pi s)\,ds$$
$$= -\frac{1}{20}i\sqrt{\frac{\pi}{2}}e^{-\frac{1}{800}\pi n(\pi n+400i)}\left(e^{i\pi n}-1\right)\left(\operatorname{erf}\left(\frac{200-i\pi n}{20\sqrt{2}}\right)+\operatorname{erf}\left(\frac{200+i\pi n}{20\sqrt{2}}\right)\right),$$

where $g \in C[0,1]$ and $\operatorname{erf}(z)$ is the error function given by $\operatorname{erf}(z) = \frac{1}{\sqrt{\pi}}\int_0^z e^{-s^2}\,ds$.

Fig. 1 depicts the results for various values of α at $T = 5$, along with the mesh movement behaviour specifically for $\alpha = 1.5$ at $T = 5$ with the initial condition (39).

To assess the performance of the adaptive moving mesh algorithm, we define the relative error as

$$e_r = \frac{\|U-u\|_\infty}{\|u\|_\infty},$$

where the U is the numerical approximation of u at time T. Table 1 presents the relative errors e_r and the corresponding convergence orders for $\alpha = 1.1, 1.3, 1.5, 1.8$ in the l_∞-norm with various numbers of mesh points N. In Fig. 3, we compare the convergence rate of between the uniform L2 and the adaptive moving L2. It shows clearly that both two meshes are numerically convergent for N increasing, and in the early stages of increasing the number of mesh points, adaptive moving L2 exhibit a faster convergence rate compared to uniform L2. To further evaluate the mesh quality, we calculated the local and global quasi-uniformity measures, as shown in Fig. 2, providing numerical evidence that no node-crossing(edges connected two nodes intersect or cross each other) occurred during the simulation. Additionally, the local quasi-uniformity L approaches 1 as N increases, indicating that the meshes used in the simulations are well-smoothed and redistributed. These findings demonstrate the effectiveness of the moving mesh approach in maintaining high mesh quality and avoiding mesh distortion.

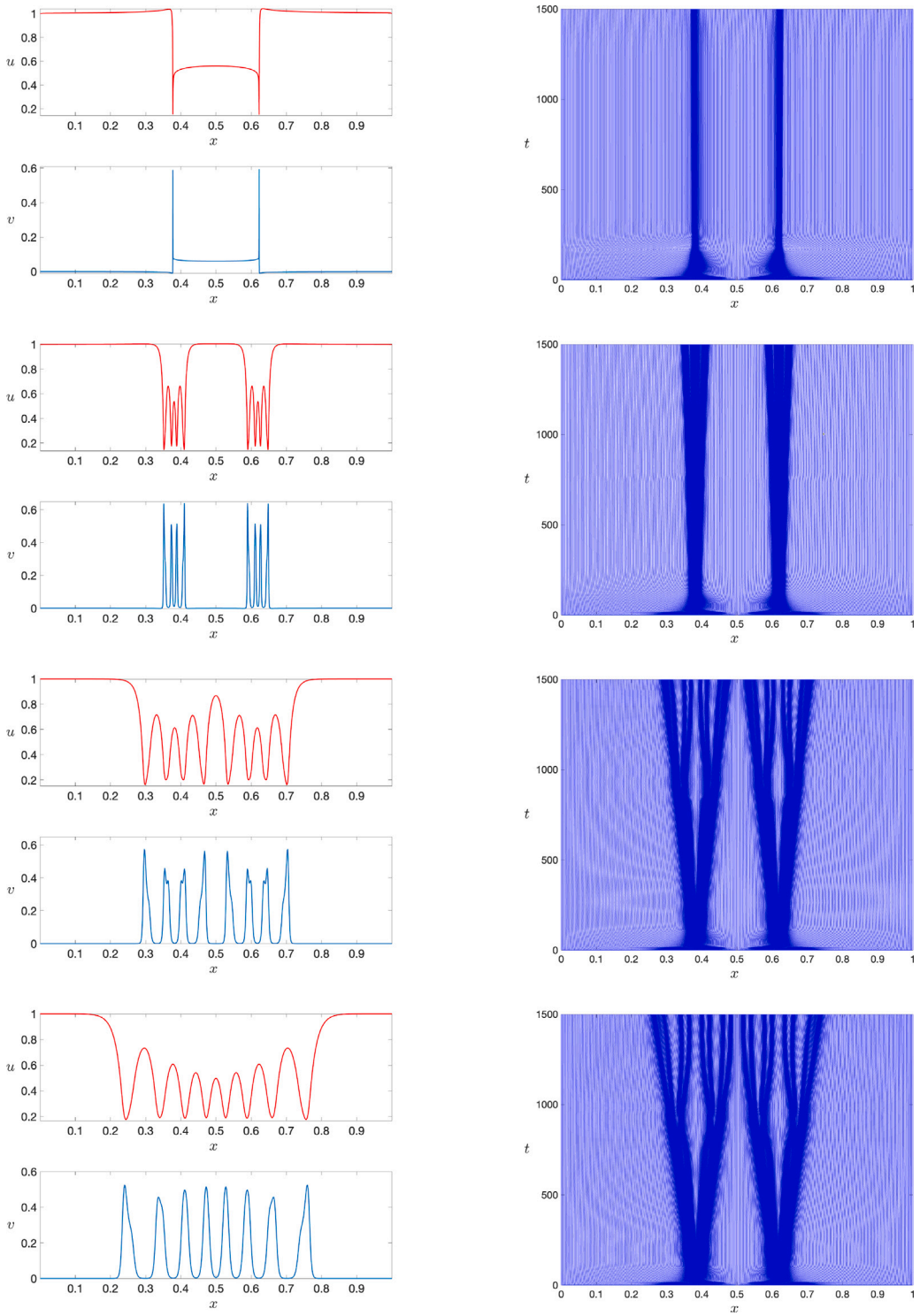

Fig. 7. Numerical solutions of (46)–(48) for self-replicating pattern within the interval $\Omega = (0, 1)$ with $r_u = 10^{-5}, r_v = 10^{-6}, F = 0.024, \kappa = 0.06$ and $\alpha = 1.1, 1.5, 1.8, 2$ at $T = 1500$, using a 500-moving mesh.

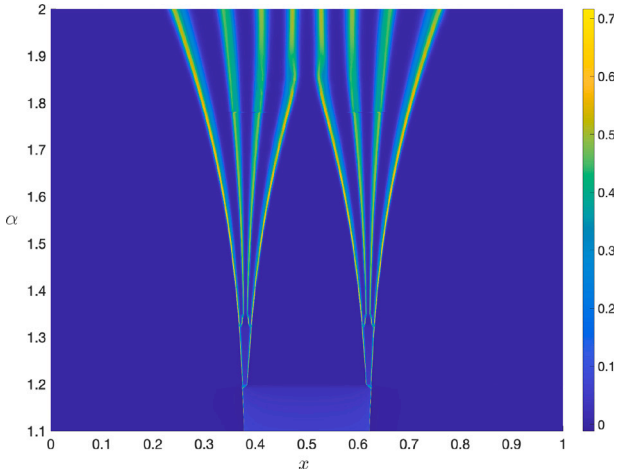

Fig. 8. Self-replicating patterns of the fractional Gray–Scott system (46)–(48) were computed for values of α ranging from 1.1 to 2 at time $T = 1500$, using a 500-moving mesh.

Table 1
The relative errors and convergence order of (38) using the L2 method on uniform and adaptive meshes, each with 40, 80, 160, and 320 mesh points, are computed. The computations are performed for α values of 1.1, 1.3, 1.5, and 1.8 at time $T = 5$, employing the l^∞ norm.

N	$\alpha = 1.1$				$\alpha = 1.3$			
	Uniform	Order	Adaptive	Order	Uniform	Order	Adaptive	Order
40	0.0802		0.0441		0.0403		0.0245	
80	0.0450	0.8337	0.0231	0.9329	0.0229	0.8254	0.0121	1.0178
160	0.0239	0.9129	0.0117	0.9814	0.0121	0.9203	0.0060	1.0120
320	0.0125	0.9351	0.0056	1.0630	0.0063	0.9416	0.0029	1.0489
N	$\alpha = 1.5$				$\alpha = 1.8$			
	Uniform	Order	Adaptive	Order	Uniform	Order	Adaptive	Order
40	0.0288		0.0196		0.0101		0.0109	
80	0.0168	0.7776	0.0097	1.0148	0.0066	0.6138	0.0059	0.9353
160	0.0090	0.9005	0.0049	0.9852	0.0036	0.8745	0.0029	1.0255
320	0.0046	0.9683	0.0024	1.0297	0.0018	1.0000	0.0013	1.1635

6.2. The space-fractional heat equation with a source term

We consider the following fractional heat equation with a source term:

$$\begin{cases} \dfrac{\partial u}{\partial t} = -(-\Delta)^{\alpha/2} u + f(x,t), & x \in (-1,1), \\ u = 0 \quad \text{on} \quad \mathbb{R}\backslash\Omega, \end{cases} \qquad t \in [0,T], \tag{41}$$

where the non-homogeneous function $f(x,t)$ is defined as

$$f(x,t) = e^t x \left(\frac{2^\alpha(\alpha+1)\Gamma\left(\frac{\alpha+1}{2}\right)\Gamma\left(\frac{1}{2}\left(\alpha^3+\alpha+6\right)\right) {}_2F_1\left(\frac{\alpha+3}{2}, -\frac{\alpha^3}{2}-2; \frac{3}{2}; x^2\right)}{\sqrt{\pi}\Gamma\left(\frac{\alpha^3}{2}+3\right)} - \left(1-x^2\right)^{\frac{1}{2}\left(\alpha^3+\alpha+4\right)} \right), \tag{42}$$

where the Gauss hypergeometric function ${}_2F_1(p_1,p_2;q;z) = \sum_{n=0}^{\infty} \frac{(p_1)_m (p_2)_m}{(q)_m} \frac{z^m}{m!}$ with $(x)_m = \frac{\Gamma(x+m)}{\Gamma(x)}$ [36]. The analytical solution to Eq. (41) has been studied in previous works [37–39]., which is

$$u(x,t) = e^t x \left(1-x^2\right)^{\frac{1}{2}\left(\alpha^3+\alpha+4\right)}, \ (x,t) \in (-1,1) \times [0,T], \tag{43}$$

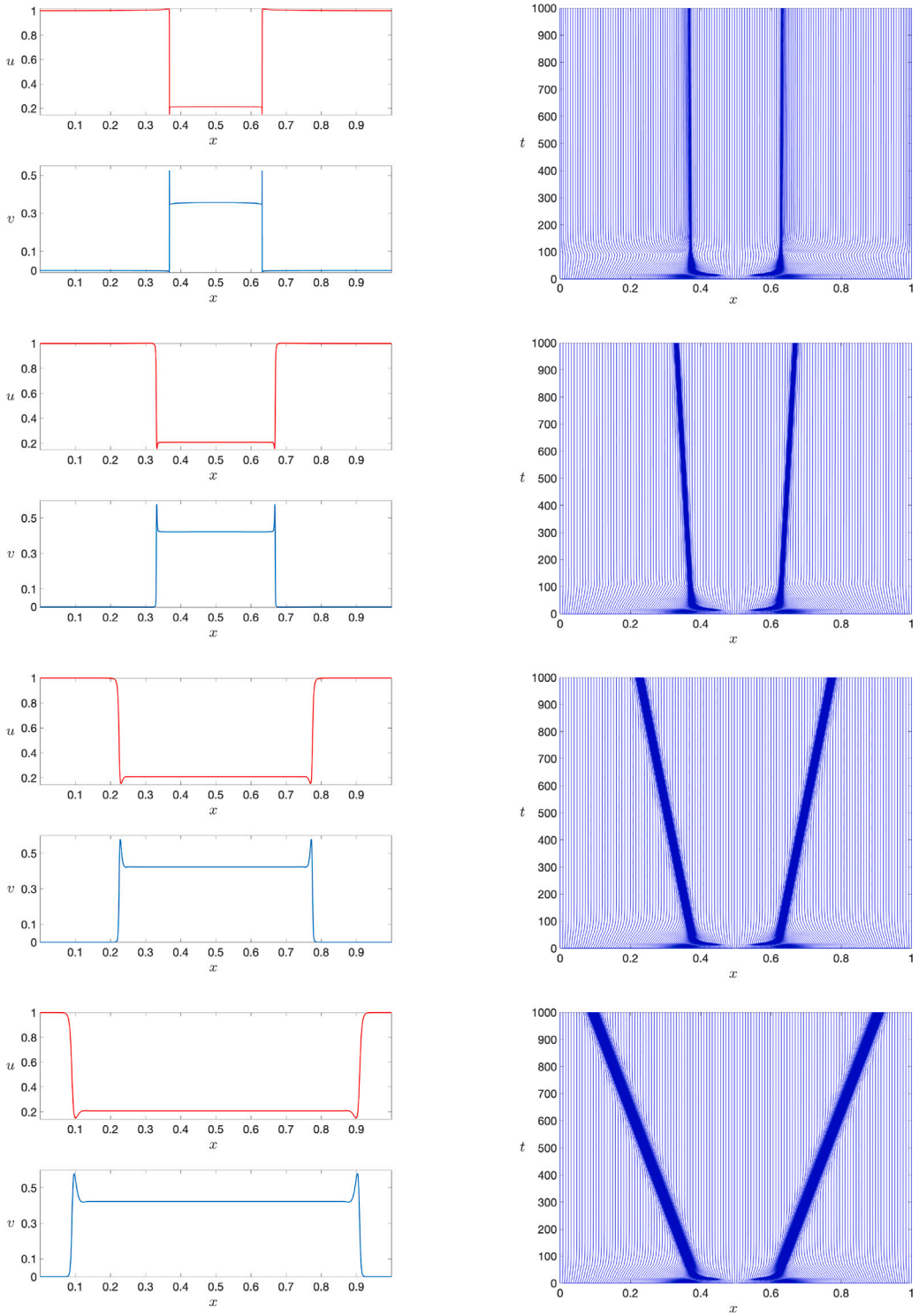

Fig. 9. Numerical simulations of (46)–(48) for travelling wave pattern within the interval $\Omega = (0, 1)$ with parameters $r_u = 2\times10^{-6}$, $r_v = 10^{-6}$, $F = 0.047$, $\kappa = 0.041$, and $\alpha = 1.1, 1.5, 1.8, 2$ at $T = 1000$, using a 240-moving mesh.

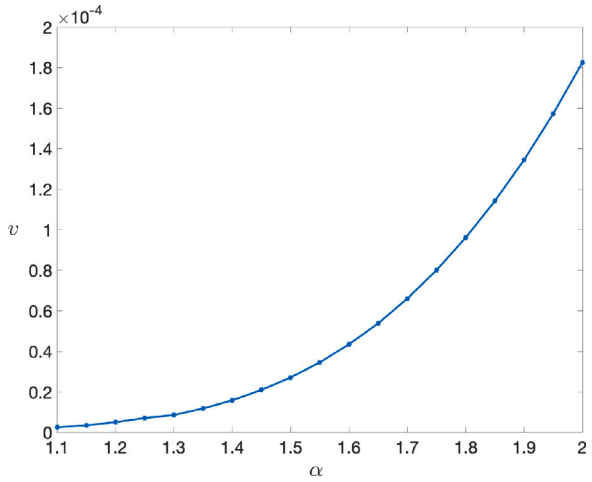

Fig. 10. Propagating speed of travelling waves for α from 1.1 to 2.

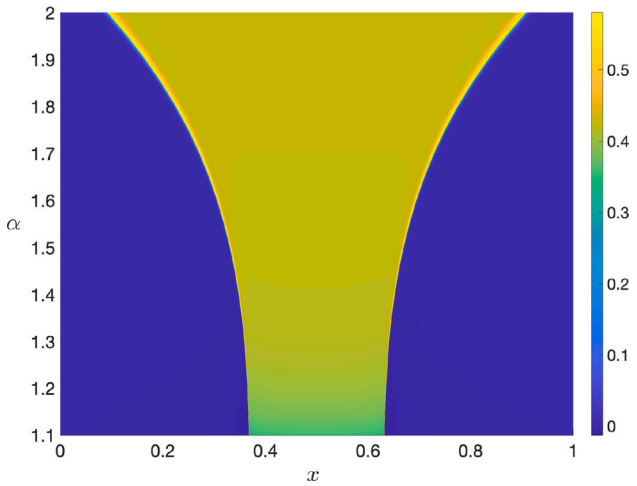

Fig. 11. Travelling wave patterns of the fractional Gray–Scott system (46)–(48) were computed for values of α ranging from 1.1 to 2 at time $T = 1000$, using a 240-moving mesh.

and therefore, we simply take the initial condition as

$$u(x,0) = x\left(1-x^2\right)^{\frac{1}{2}(\alpha^3+\alpha+4)}. \tag{44}$$

For the space-fractional PDE, Siwei Duo et al. presents a finite difference method for discretizing the fractional Laplacian in hypersingular integral form and exhibits consistent convergence behaviour verified through numerical examples for various $\alpha \in (0,2)$ when applied to solve the stationary fractional Laplacian equation with source term [37]. Fig. 4 shows the numerical solution using $\alpha = 1.1,\ 1.5,\ 1.8$ at the final time $T = 1$.

Table 2 presents the relative errors e_r and the corresponding convergence orders for $\alpha = 1.1, 1.3, 1.5, 1.8$ in the l_∞-norm with various numbers of mesh points N. Similarly to the first case, Fig. 5 presents estimates of local and global quasi-uniformity, showing that the mesh points are well-smoothed with no mesh distortion. And in Fig. 6, the convergence rates of the uniform L2 and the adaptive moving L2 are compared, showing that adaptive moving L2 performs better numerical convergence in the early stages when more mesh points are adopted.

From Fig. 4, it can be observed that the numerical solutions are less accurate when α is near 1, one reason is that in the L2-method, fewer points are available to estimate those derivatives near the boundary $\partial\Omega$, resulting in lower accuracy. For example, the left-derivative at the first mesh point is roughly estimated as

$${}_C D^{\alpha}_{0,x_1} u(x_1,t) = \frac{2}{\Gamma(3-\alpha)}\left(\frac{u_0(t)}{(x_1-x_0)(x_2-x_0)} - \frac{u_1(t)}{(x_2-x_1)(x_1-x_0)} + \frac{u_2(t)}{(x_2-x_1)(x_2-x_0)}\right)(x_1-x_0)^{2-\alpha}. \tag{45}$$

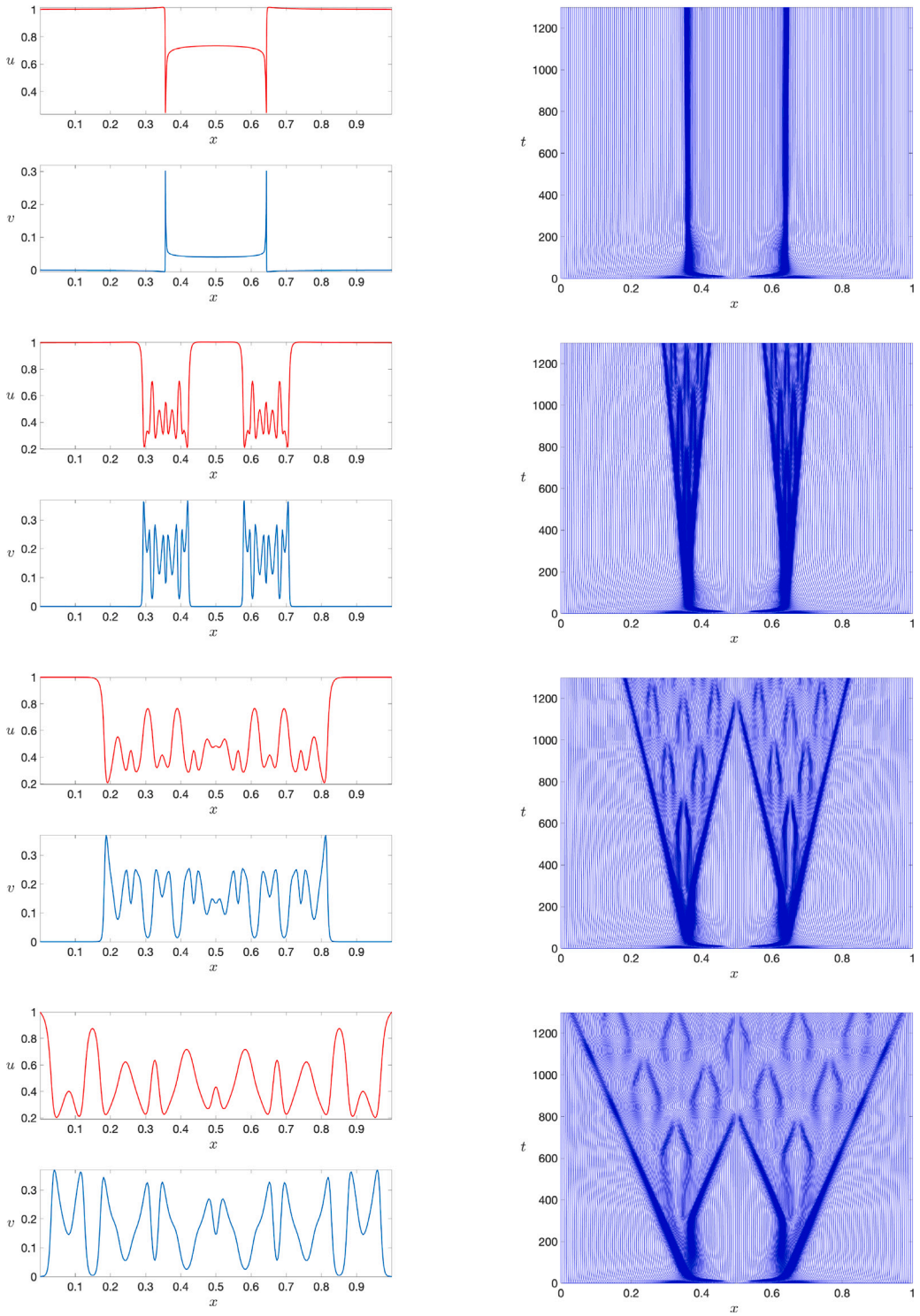

Fig. 12. Numerical simulations of (46)–(48) for chaotic pattern within the interval $\Omega = (0, 1)$ with parameters $r_u = 4 \times 10^{-6}, r_v = 10^{-6}, F = 0.022, \kappa = 0.05$ and $\alpha = 1.1, 1.5, 1.8, 2$ at $T = 1300$, using a 300-moving mesh.

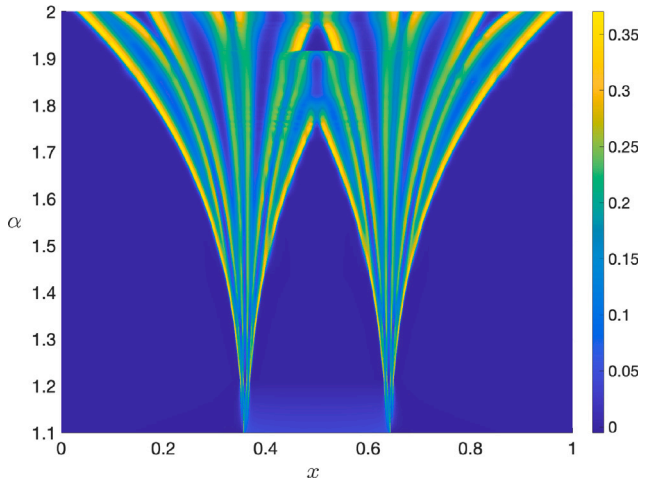

Fig. 13. Chaotic patterns of the fractional Gray–Scott system (46)–(47) were computed for values of α ranging from 1.1 to 2 at time $T = 1300$, using a 300-moving mesh. One possible bifurcation occurs between α-values of 1.7 and 1.8.

Table 2
The relative errors and convergence order of (41) using the L2 method on uniform and adaptive meshes, each with 40, 80, 160, and 320 mesh points, are computed. The computations are performed for α values of 1.1, 1.3, 1.5, and 1.8 at time $T = 1$, employing the l^∞ norm.

N	$\alpha = 1.1$				$\alpha = 1.3$			
	Uniform	Order	Adaptive	Order	Uniform	Order	Adaptive	Order
40	0.3496		0.2959		0.1514		0.1174	
80	0.2142	0.7063	0.1726	0.7773	0.0836	0.8568	0.0619	0.9234
160	0.1206	0.8285	0.0948	0.8642	0.0440	0.9260	0.0318	0.9609
320	0.0642	0.9092	0.0497	0.9311	0.0226	0.9612	0.0161	0.9820
N	$\alpha = 1.5$				$\alpha = 1.8$			
	Uniform	Order	Adaptive	Order	Uniform	Order	Adaptive	Order
40	0.0864		0.0621		0.0279		0.0192	
80	0.0471	0.8747	0.0321	0.9531	0.0165	0.7517	0.0101	0.9369
160	0.0247	0.9301	0.0163	0.9772	0.0089	0.8941	0.0052	0.9506
320	0.0126	0.9688	0.0083	0.9806	0.0046	0.9397	0.0027	0.9725

Same problem for the right-derivative on the other side of the boundaries. When we combine these two derivatives for calculating the fractional Laplacian in practical computation, the term $-\frac{1}{\cos(\alpha\pi/2)}$, significantly amplifies the error when $\alpha \downarrow 1$. Only when more mesh points used near the boundaries or $u|_R = u|_L = u_x|_R = u_x|_L = 0$ the L2-method can work well. Consistent with our experience, this problem will be resolved with the adoption of a larger number of mesh points N, see Table 2.

6.3. The space-fractional Gray–Scott(G–S) model

Having gained confidence from successfully applying the numerical scheme to two known fractional Laplacian equations, next we proceed to numerically solve the equations represented by the Gray–Scott system involved the fractional Laplacian term, which is given by

$$\begin{cases} \dfrac{\partial u}{\partial t} = -r_u(-\Delta)^{\frac{\alpha}{2}} u - uv^2 + F(1-u), \\ \dfrac{\partial v}{\partial t} = -r_v(-\Delta)^{\frac{\alpha}{2}} v + uv^2 - (F+\kappa)v, \end{cases} \quad (x,t) \in \mathbb{R} \times [0,T], \tag{46}$$

where u and v are the concentrations of two chemical components in reaction–diffusion process, that are inhibitor and called activator, respectively.

Well-posedness: The well-posedness of the fractional G–S model has been studied in detail in [40]. For the fractional order $1 < \alpha \leq 2$, the solution of (46) in a finite domain Ω can be bounded under some specific conditions: the solutions $u(t), v(t) \in H_0^{\frac{1}{2}}(\Omega)$ for any initial conditions $u_0, v_0 \in H_0^{\frac{1}{2}}(\Omega)$, where $H_0^{\frac{1}{2}}(\Omega) := C_0^\infty(\Omega) \cap \{u \in L^2(\Omega) : \frac{u(x)-u(y)}{|x-y|^{\frac{1}{2}+s}} \in L^2(\Omega)\}$. Therefore, we take the boundary

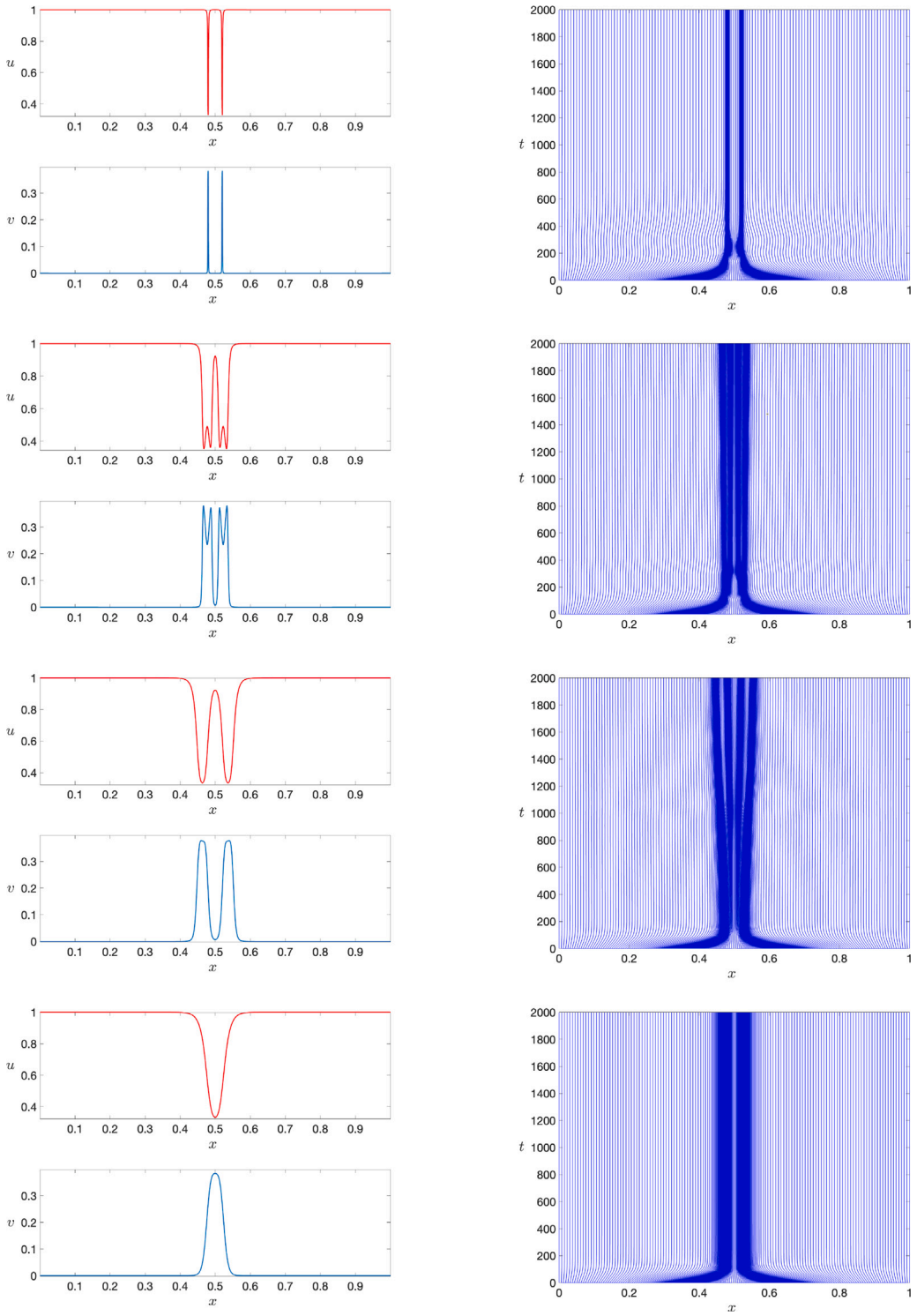

Fig. 14. Numerical simulations of (46)–(48) include the standing wave pattern and self-replicating pattern within the interval $\Omega = (0, 1)$, with parameters $r_u = 10^{-5}, r_v = 5 \times 10^{-6}, F = \kappa = \frac{1}{16}$ and $\alpha = 1.1, 1.5, 1.8, 2$ at $T = 2000$, using a 240-moving mesh.

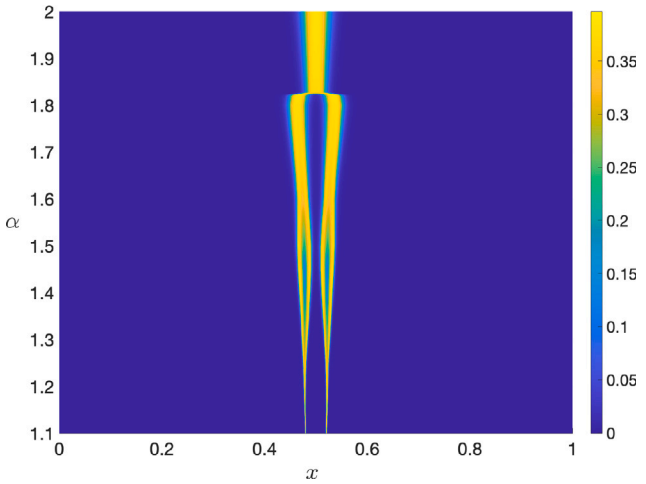

Fig. 15. The evolutionary process, including both standing wave and self-replicating patterns of the fractional Gray–Scott system (46)–(48), was computed for values of α ranging from 1.1 to 2 at time $T = 2000$, using a 240-moving mesh. One possible bifurcation occurs between α-values of 1.8 and 1.9.

conditions as following:

$$u = 0 \text{ and } v = 0 \text{ on } \mathbb{R}\backslash\Omega. \tag{47}$$

The ordinary (integer-order) Gray–Scott model has been extensively studied by many researchers [21,22,41] The diffusion coefficients satisfy $r_u \geq 0, r_v \geq 0$. The parameters F, κ are positive constants representing feed rate and decay rate, respectively. This system has the spatially uniform steady states $(u_*, v_*) = (1, 0)$ for all values of F and κ. In addition, there also exist two steady states (u_+, v_-) and (u_-, v_+) when $F \geq 4(F+\kappa)^2$

$$(u_+, v_-) = \left(\frac{1}{2}(1+\sqrt{A}), \frac{F}{2(F+\kappa)}(1-\sqrt{A})\right), \quad (u_-, v_+) = \left(\frac{1}{2}(1-\sqrt{A}), \frac{F}{2(F+\kappa)}(1+\sqrt{A})\right),$$

where $A = 1 - \frac{4(F+\kappa)^2}{F}$. As a result, we can get a saddle–node bifurcation for $\kappa_c = -F + \frac{1}{2}\sqrt{F}$ and the critical feed rate $F_c = \frac{\sqrt{\kappa}(1-2\sqrt{\kappa}) - \sqrt{\kappa(1-4\sqrt{\kappa})}}{2}$, $0 \leq \kappa \leq \kappa_c$. For a detailed other analysis of the dynamical behaviour of the classical(integer-order) G–S model are referring to [21,40].

In this section, we focus on three patterns: self-replication, travelling and a possible bifurcation point between stable and self-replication with the following initial condition

$$[u(x,0), v(x,0)]^\intercal = [1 - \frac{1}{2}\sin^{10}(\pi x), \frac{1}{4}\sin^{10}(\pi x)]^\intercal. \tag{48}$$

In the practical computing, we introduced the variable w as $w = u - 1$ to give a aligned boundary conditions with the second equation and to avoid boundary terms of the Laplacian term being taken into account by Theorem 2.2. Subsequently, Eqs. (46)–(48) are modified by employing (w, v) as:

$$\begin{cases} \dfrac{\partial w}{\partial t} = -r_w(-\Delta)^{\frac{\alpha}{2}} w - (w+1)v^2 + F(w), \ (x,t) \in \mathbb{R} \times [0,T] \\ \dfrac{\partial v}{\partial t} = -r_v(-\Delta)^{\frac{\alpha}{2}} v + (w+1)v^2 - (F+\kappa)v, \\ w = 0 \text{ and } v = 0 \text{ on } \mathbb{R}\backslash\Omega, \\ [w(x,0), v(x,0)]^\intercal = [-\frac{1}{2}\sin^{10}(\pi x), \frac{1}{4}\sin^{10}(\pi x)]^\intercal. \end{cases} \tag{49}$$

6.3.1. Self-replicating patterns

Based on [21,22], we choose the parameters $r_w = 10^{-5}, r_v = 10^{-6}, F = 0.024, \kappa = 0.06$, the numerical solution and the corresponding trajectory of the mesh movement towards Eq. (49) are depicted in Fig. 7.

Fig. 8 shows the evolution of the fractional Gray–Scott equations with α at the final time $T = 1500$.

6.3.2. Travelling waves

By choosing the parameters $r_w = 2\times10^{-6}, r_v = 10^{-6}, F = 0.047, \kappa = 0.041$, the numerical solution and the corresponding trajectory of the mesh movement towards Eq. (49) are depicted in Fig. 9. The propagating speed of waves for α values arranging from 1.1 to 2 is also depicted in Fig. 10.

Fig. 11 shows the evolution of the fractional Gray–Scott equations with α at the final time $T = 1000$.

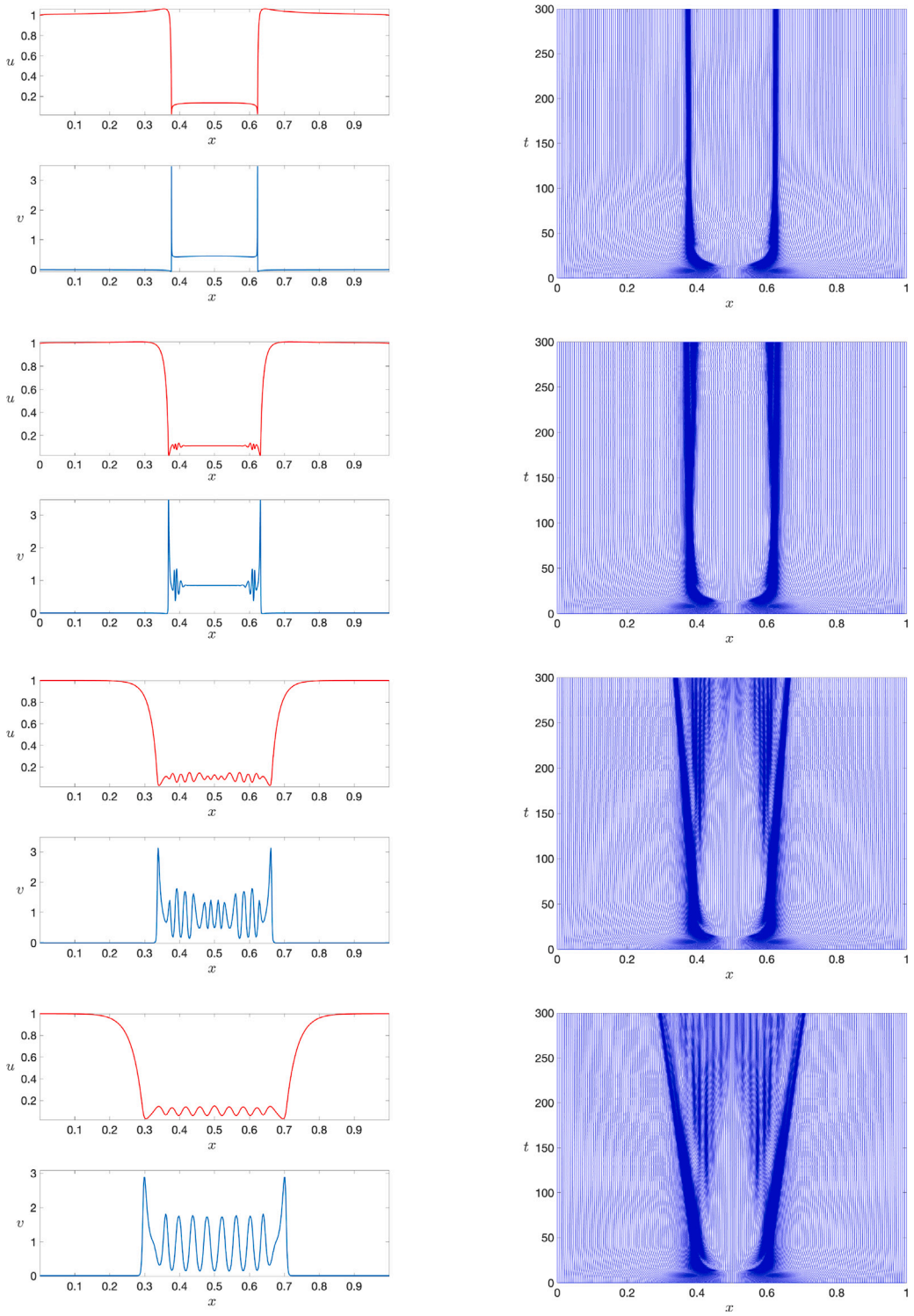

Fig. 16. Numerical simulations of (46)–(48) include both travelling wave and self-replicating patterns within the interval $\Omega = (0, 1)$, with parameters $r_u = 4\times10^{-4}$, $r_v = 2\times10^{-6}$, $F = 0.095$, $\kappa = 0.001$, and $\alpha = 1.2, 1.5, 1.8, 2$ at $T = 300$, using a 300-moving mesh.

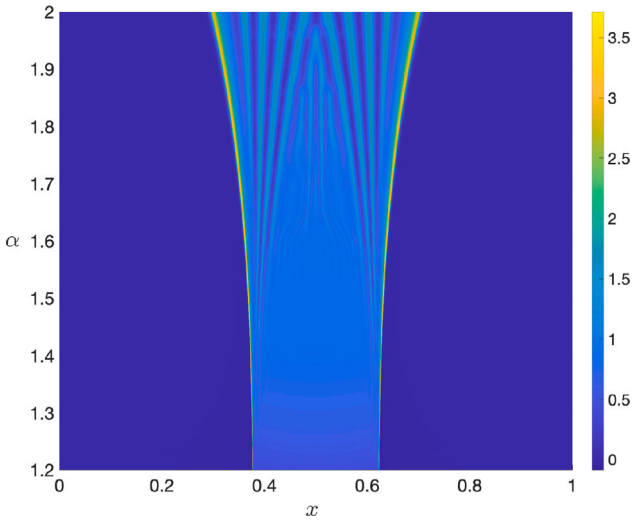

Fig. 17. The evolutionary process, including both self-replicating and travelling patterns of the fractional Gray–Scott system (46)–(47) were computed for values of α ranging from 1.2 to 2 at time T = 300, utilizing a 300-moving mesh. Two possible bifurcation can be observed between α-values of 1.2 and 1.3, 1.9 and 2.

6.3.3. Chaotic solutions

By choosing the parameters $r_w = 4 \times 10^{-6}, r_v = 2 \times 10^{-6}, F = 0.022, \kappa = 0.05$, the numerical solution and the corresponding trajectory of the mesh movement towards Eq. (49) are depicted in Fig. 12.

Fig. 13 shows the evolution of the fractional Gray–Scott equations with varying α at the final time $T = 1300$. One possible bifurcation may exist between α values of 1.7 and 1.8, corresponding to the moment when two travelling fronts meet.

6.3.4. Evolutionary process from standing wave to self-replicating pattern

The main feature of the associated ODE of (46) is that it has a Bogdanov–Takens point at $(\kappa, F) = (\frac{1}{16}, \frac{1}{16})$ together with a stable critical point $(1, 0)$. A Bogdanov–Takens point is a singularity of codim 2, where Saddle-Node and Hopf bifurcations merge into two-dimensional parameter space (κ, F) [41], and most of the interesting PDE dynamics appears near these two bifurcation lines for the classical Gray–Scott model. Thus, we applied these two values to the fractional model (46) and observed a possible bifurcation point by choosing the parameters $r_w = 10^{-5}, r_v = 5 \times 10^{-6}, F = \kappa = \frac{1}{16}$. Under this selection of parameters, the kinetics for the Gray–Scott model changed from self replication to stable with α increasing, a possible bifurcation point could be existed between 1.8 and 1.9. This is presented in Fig. 15. And the numerical solutions and the corresponding trajectory of the mesh movement towards Eq. (49) are depicted in Fig. 14.

6.3.5. Evolutionary process from travelling wave to self-replicating pattern

By choosing the parameters $r_w = 4 \times 10^{-4}, r_v = 2 \times 10^{-6}, F = 0.095, \kappa = 0.001$, the numerical solution and the corresponding trajectory of the mesh movement towards Eq. (49) are depicted in Fig. 16. In this experiment, we started with $\alpha = 1.2$ instead of $\alpha = 1.1$ because the derivatives undergo drastic changes within a very small region, almost reaching discontinuity. Therefore, more mesh points are needed to achieve more accurate solutions in $\alpha \downarrow 1$-cases. The studies conducted in [42,43] confirm the loss of periodicity in the fractional time derivative, that is periodicity is not transferred by fractional integral or derivative, with the exception of the zero function. In this work, we numerically present that periodicity diminishes in space as α decreases from 2 and transforms into a travelling wave as α approaches 1, two possible bifurcation points could be existed between 1.2 and 1.3, 1.9 and 2, see Fig. 17.

7. Conclusions

In conclusion, this paper introduced an innovative method for computing the fractional Laplacian using Riemann–Liouville derivatives, incorporating a boundary condition of $u = 0$ in $\mathbb{R}\backslash\Omega$. Notably, for smooth functions $u \in S(\Omega)$, the proposed approach simplifies the Riemann–Liouville derivatives to the Caputo derivatives due to the vanishing boundaries. The extension of the L2 method to non-uniform meshes was presented, accompanied by a proof of its numerical consistency. The flexibility of the non-uniform L2 method in constructing meshes allows users to choose different mesh updating techniques, enhancing numerical performance for various problems.

The adaptive moving finite differences method was employed for spatial mesh generation, offering adaptability at each time step through grid reallocation based on the previous solution. The choice of MMPDE5 for mesh movement, based on the equidistribution principle, proved effective. However, initial observations revealed rapid mesh movement, particularly challenging to discern in specific cases. The numerical scheme's feasibility was validated through two experiments, demonstrating improved results.

The primary objective of this study was to solve space-fractional PDE problems in one dimension and apply the proposed numerical method to a nonlinear fractional PDE problem, *i.e.*, the fractional Gray–Scott model. Numerical experiments focused on the fractional Gray–Scott revealed three patterns including patterns of self-replication, travelling, chaotic and two distinct evolutionary processes from self-replicated pattern to standing wave and from travelling wave to self-replication pattern.

In future work, we will attempt to extend this method to the two-dimensional case. The pattern formation of the two-dimensional space-fractional Gray–Scott model has been an important topic, and some studies have already proposed related numerical algorithms. We will compare the numerical performance of these methods with the adaptive L2 method. Additionally, we plan to apply this method to other nonlinear models, such as the space-fractional Cahn–Hilliard equation and the time–space fractional Schrödinger equation.

CRediT authorship contribution statement

P. Yuan: Writing – original draft, Visualization, Software, Methodology, Investigation, Formal analysis, Data curation, Conceptualization. **P.A. Zegeling:** Writing – review & editing, Supervision, Project administration, Conceptualization.

Declaration of competing interest

The authors declare that they have no known competing financial interests or personal relationships that could have appeared to influence the work reported in this paper.

Data availability

Data will be made available on request.

Acknowledgement

Pu Yuan would like to acknowledge the support of China Scholarship Council (Grant No. 202207720037).

References

[1] Failla G, Zingales M. Advanced materials modelling via fractional calculus: challenges and perspectives. Phil Trans R Soc A 2020;378(2172):20200050.
[2] Kilbas AA, Srivastava HM, Trujillo JJ. Theory and applications of fractional differential equations, vol. 204, Elsevier; 2006.
[3] Oldham K, Spanier J. The fractional calculus theory and applications of differentiation and integration to arbitrary order. Elsevier Science; 1974.
[4] Gorenflo R, Mainardi F. Random walk models approximating symmetric space-fractional diffusion processes. In: Problems and methods in mathematical physics: the Siegfried Prössdorf memorial volume proceedings of the 11th TMP. Springer; 2001, p. 120–45.
[5] Lischke A, Pang G, Gulian M, Song F, Glusa C, Zheng X, et al. What is the fractional Laplacian? A comparative review with new results. J Comput Phys 2020;404:109009.
[6] Bonito A, Borthagaray JP, Nochetto RH, Otárola E, Salgado AJ. Numerical methods for fractional diffusion. Comput Vis Sci 2018;19(5–6):19–46.
[7] Bogdan K, Burdzy K, Chen Z-Q. Censored stable processes. Probab Theory Related Fields 2003;127:89–152.
[8] Guan Q-Y, Ma Z-M. Boundary problems for fractional Laplacians. Stoch Dyn 2005;5(03):385–424.
[9] Yang Q, Liu F, Turner I. Numerical methods for fractional partial differential equations with Riesz space fractional derivatives. Appl Math Model 2010;34(1):200–18.
[10] Liu F, Anh V, Turner I. Numerical solution of the space fractional Fokker–Planck equation. J Comput Appl Math 2004;166(1):209–19.
[11] Li C, Zeng F. Numerical methods for fractional calculus, vol. 24. 1st ed. CRC Press; 2015.
[12] Lyu P, Vong S. A nonuniform L2 formula of Caputo derivative and its application to a fractional Benjamin–Bona–Mahony-type equation with nonsmooth solutions. Numer Methods Partial Differential Equations 2020;36(3):579–600.
[13] Alikhanov AA, Huang C. A high-order L2 type difference scheme for the time-fractional diffusion equation. Appl Math Comput 2021;411:126545.
[14] Huang W, Ren Y, Russell RD. Moving mesh partial differential equations (MMPDEs) based on the equidistribution principle. SIAM J Numer Anal 1994;31(3):709–30.
[15] Huang W, Russell RD. Adaptive moving mesh methods, vol. 174, Springer Science & Business Media; 2010.
[16] Dorfi E, Drury L. Simple adaptive grids for 1-D initial value problems. J Comput Phys 1987;69(1):175–95.
[17] Huang W, Russell RD. Moving mesh strategy based on a gradient flow equation for two-dimensional problems. SIAM J Sci Comput 1998;20(3):998–1015.
[18] Huang W. Practical aspects of formulation and solution of moving mesh partial differential equations. J Comput Phys 2001;171(2):753–75.
[19] Lee K-J, McCormick WD, Pearson JE, Swinney HL. Experimental observation of self-replicating spots in a reaction–diffusion system. Nature 1994;369(6477):215–8.
[20] Pearson JE. Complex patterns in a simple system. Science 1993;261(5118):189–92.
[21] Doelman A, Kaper TJ, Zegeling PA. Pattern formation in the one-dimensional Gray–Scott model. Nonlinearity 1997;10(2):523.
[22] Reynolds WN, Pearson JE, Ponce-Dawson S. Dynamics of self-replicating patterns in reaction diffusion systems. Phys Rev Lett 1994;72(17):2797.
[23] Samko SG, Kilbas AA, Marichev OI. Fractional integrals and derivatives: Theory and applications. 1993.
[24] Stinga PR, Torrea JL. Extension problem and Harnack's inequality for some fractional operators. Comm Partial Differential Equations 2010;35(11):2092–122.
[25] Di Nezza E, Palatucci G, Valdinoci E. Hitchhiker's guide to the fractional Sobolev spaces. Bull Sci Math 2012;136(5):521–73.
[26] King FW. Hilbert transforms: Volume 1. Encyclopedia of mathematics and its applications, vol. 1, Cambridge University Press; 2009.
[27] Cayama J, Cuesta CM, de la Hoz F. A pseudospectral method for the one-dimensional fractional Laplacian on $\mathbb{R}$. Appl Math Comput 2021;389:125577.
[28] De Boor C. Good approximation by splines with variable knots. II. In: Conference on the numerical solution of differential equations: dundee 1973. Springer; 2006, p. 12–20.
[29] Huang W, Ren Y, Russell RD. Moving mesh methods based on moving mesh partial differential equations. J Comput Phys 1994;113(2):279–90.
[30] Huang W, Sun W. Variational mesh adaptation II: error estimates and monitor functions. J Comput Phys 2003;184(2):619–48.

[31] Furzeland R, Verwer J, Zegeling P. A numerical study of three moving-grid methods for one-dimensional partial differential equations which are based on the method of lines. J Comput Phys 1990;89(2):349–88.
[32] Shampine LF. Solving $0 = F(t, y(t), y'(t))$ in Matlab. J Numer Math 2002;10(4):291–310.
[33] Franz S, Kopteva N. Pointwise-in-time a posteriori error control for higher-order discretizations of time-fractional parabolic equations. J Comput Appl Math 2023;427:115122.
[34] Kautsky J, Nichols N. Equidistributing meshes with constraints. SIAM J Sci Stat Comput 1980;1(4):499–511.
[35] Huang W, Russell RD. Analysis of moving mesh partial differential equations with spatial smoothing. SIAM J Numer Anal 1997;34(3):1106–26.
[36] Srivastava H, Agarwal P, Jain S. Generating functions for the generalized Gauss hypergeometric functions. Appl Math Comput 2014;247:348–52.
[37] Duo S, van Wyk HW, Zhang Y. A novel and accurate finite difference method for the fractional Laplacian and the fractional Poisson problem. J Comput Phys 2018;355:233–52.
[38] lomiej Dyda B. Fractional calculus for power functions and eigenvalues of the fractional Laplacian. Fract Calc Appl Anal 2012;15(4):536–55.
[39] Gutleb TS, Papadopoulos IP. Explicit fractional Laplacians and Riesz potentials of classical functions. 2023, arXiv preprint arXiv:2311.10896.
[40] Wang T, Song F, Wang H, Karniadakis GE. Fractional Gray–Scott model: well-posedness, discretization, and simulations. Comput Methods Appl Mech Engrg 2019;347:1030–49.
[41] Nishiura Y, Ueyama D. Spatio-temporal chaos for the Gray–Scott model. Physica D 2001;150(3–4):137–62.
[42] Kaslik E, Sivasundaram S. Non-existence of periodic solutions in fractional-order dynamical systems and a remarkable difference between integer and fractional-order derivatives of periodic functions. Nonlinear Anal Real World Appl 2012;13(3):1489–97.
[43] Area I, Losada J, Nieto JJ. On fractional derivatives and primitives of periodic functions. In: Abstract and applied analysis, vol. 2014, Hindawi; 2014.